APPENDIX E - Digital Image Correlation Effort

Executive Summary:

Digital Image Correlation (DIC) were made on three separate TPI Composites CX-100, 9 m wind turbine blades (Sandia "Sensor Blade", LANL Blade and UMass Lowell Defect Blade). The results of the tests on the Sandia blade revealed that DIC could readily identify changes in strain and surface geometry due to cracks present in the blade after being subjected to fatigue failure. The Sandia blade tests also revealed that multiple images can be stitched together to obtain the blade geometry, deformation, and full-field strain over the entire blade area. The LANL blade served as a baseline (defect-free blade) for comparison in which DIC was used to interrogate the same six areas that possessed defects in the UMass Lowell blade. The results revealed that there was no significant increase in strain at these locations in the defect-free blade. DIC was also used to interrogate the six different locations that possessed defects in the UMass Lowell blade. The results indicate that DIC can be used as a full-field inspection technique to identify defects (via strain amplification) and monitor the progression of crack growth or structural changes. The primary results are described in detail in the following references, but are summarized in this Report Appendix.

1. LeBlanc, B., Niezrecki, C., Avitabile, P., Sherwood, J., and Chen, J., "Surface Stitching of a Wind Turbine Blade Using Digital Image Correlation," Proceedings of IMAC-XXX, Jacksonville, FL, January 30 - February 2, 2012.

2. LeBlanc, B., Niezrecki, C., Hughes, S., Avitabile, P., Chen, J., and Sherwood, J., "Full Field Inspection of a Wind Turbine Blade Using 3D Digital Image Correlation," Proceedings of the SPIE Symposium on Smart Structures & Materials/NDE for Health Monitoring, San Diego, California, March, 2011.

3. Bruce Leblanc, Master of Science Thesis University of Massachusetts Lowell, Sept. 2011, "Non-Destructive Testing of Wind Turbine Blades with Three Dimensional Digital Image Correlation"

Overview of Digital Image Correlation

The non-destructive inspection approach within this work primarily uses three-dimensional digital image correlation. Before discussing 3D DIC in detail it is necessary to have a basic understanding of traditional digital image correlation.

1.1 DIGITAL IMAGE CORRELATION

Digital image correlation is a non-contacting measurement technique that uses images taken with a charged couple device (CCD) digital camera to track in-plane motion. An image is digitized into a certain number of pixels, each with a corresponding level of light intensity. Therefore, every digital image taken has a specific grey-level assigned to each pixel. A subset matrix of pixels on the image (typically 15x15), known as a facet, should ideally have several grey-level variations. By tracking the motion of each facet in a series of images, the in-plane displacement and strain of that facet can be calculated. When a stochastic grey-level pattern is applied in intimate contact with a structure (assuming the pattern moves directly with the

structure) the strain and displacement of each facet is directly related to the strain and displacement of the structure. A typical image with overlaid facet is shown in Figure E.1.

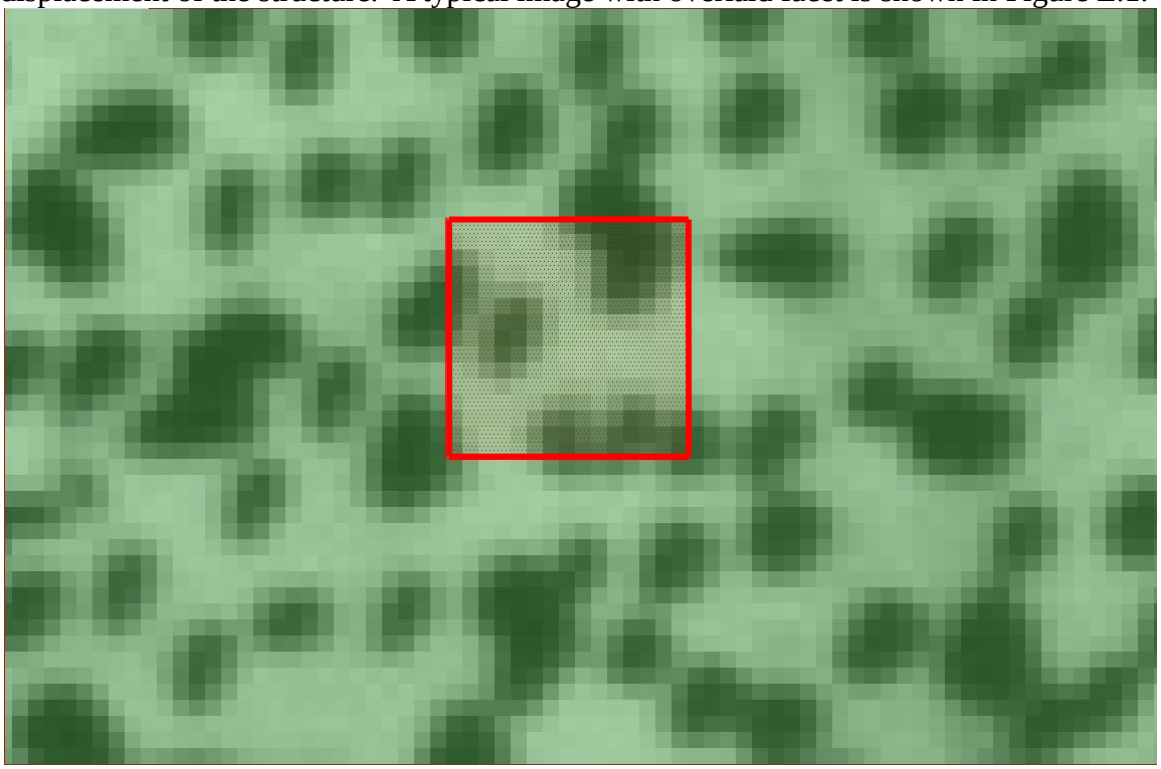

Figure E.1 Pixilated image with overlaid facet.

1.2 3D DIC / STEREO-PHOTOGRAMMETRY

3D DIC utilizes images taken simultaneously from a pair of digital cameras to track a stochastic pattern on a structure in order to provide full-field displacement and strain information for a structure. This is performed by using the principle of stereo-photogrammetry and bundle adjustment along with the standard two dimensional technique of DIC, the concepts of which are explained in detail by Bruck, et al (1).

In summary, the method of stereo-photogrammetry assumes the relative position of a pair of digital cameras with respect to each other is known through a calibration process and remains constant throughout testing. By imaging a common point with both cameras, the location of that point, with respect to the camera pair, can be triangulated in three-dimensional space. Figure E.2 displays a graphical rendition of stereo-photogrammetry.

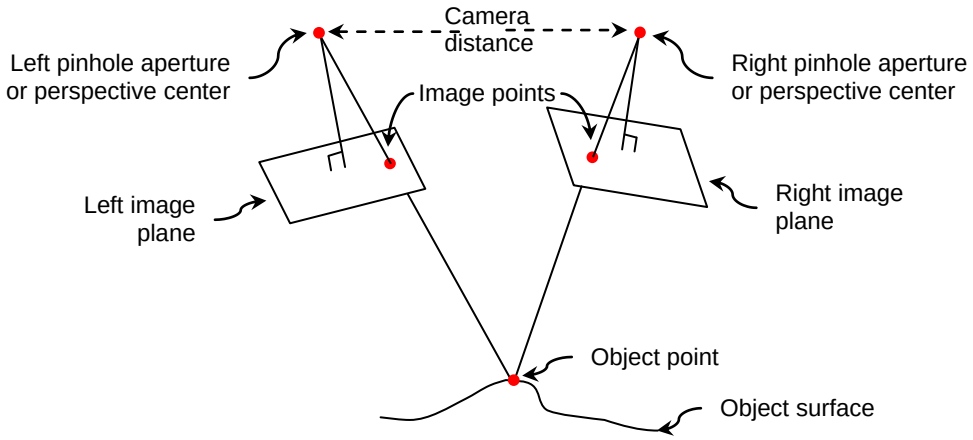

Figure E.2 Overview of stereo-photogrammetry(2).

By combining the technique of stereo-photogrammetry with traditional digital image correlation, a full-field 3D structural shape, consisting of numerous data points (on order of thousands) can be acquired. When a series of images (stages) is taken, the subsequent stages are compared to a reference stage and full-field deformations and strains can be calculated. The approach therefore provides global information about changes to the structure over the entire field of view in a snapshot. All 3D DIC work in this project was performed using ARAMIS^{TM}, a commercially available product by GOM (3).

1.3 STRAIN CALCULATION

Strain is calculated from the image stages by extracting a set of 3D points from the surface and applying the laws of continuum mechanics. The laws associated with continuum mechanics and the derivation of the finite-strain equations, shown in
Equation 2.1, has been explained in detail in many textbooks (4) and will not be redefined here. These are the main equations one would use in a DIC program to compute strain. The finite-strain equations with original coordinates x, y, z and displacements u, v, and w are:

$$\varepsilon_{xx} = \frac{\partial u}{\partial x} + \frac{1}{2}\left[\left(\frac{\partial u}{\partial x}\right)^2 + \left(\frac{\partial v}{\partial x}\right)^2 + \left(\frac{\partial w}{\partial x}\right)^2\right],$$
$$\varepsilon_{yy} = \frac{\partial v}{\partial y} + \frac{1}{2}\left[\left(\frac{\partial u}{\partial y}\right)^2 + \left(\frac{\partial v}{\partial y}\right)^2 + \left(\frac{\partial w}{\partial y}\right)^2\right], \qquad [2\text{-}1]$$
$$\varepsilon_{xy} = \frac{1}{2}\left[\frac{\partial u}{\partial y} + \frac{\partial v}{\partial x} + \left(\frac{\partial u}{\partial x}\frac{\partial u}{\partial y}\right) + \left(\frac{\partial v}{\partial x}\frac{\partial v}{\partial y}\right) + \left(\frac{\partial w}{\partial x}\frac{\partial w}{\partial y}\right)\right].$$

The process of extracting these 3D points and surface deformations from the image stages is the focus of this section. There are several main parameters used within the software to extract data from the captured image stages. These parameters are: 1) facet size, 2) facet step, 3) computation size, 4) validity quote, and 5) filtering (5).

As described previously, a facet is a subset of pixels containing several grey level variations that uniquely describes its position within the image. A facet is normally square with a size of approximately 15 by 15 pixels. However, this size may be changed depending upon the surface geometry and dot pattern measured. The center of each facet is calculated within the software providing a point location representing the coordinates of the center of the facet in

three-dimensional space. The accuracy of this 3D point location depends upon the size of the facet, however is on the order of $1/50^{th}$ of a pixel in plane, and $1/30^{th}$ of a pixel out of plane (5).

An initial single facet, known as the start point, is defined for each image stage. This unique facet is first defined for one of the stereo-cameras, and needs to be recognized by the other to calculate the position in 3D space correctly. Once this point is defined, the remainder of the field of view that is visible within both stereo-images is divided into adjacent (sometimes overlapping) facets. The number of pixels between each sequential facet is known as the **facet step**, see Figure E.3.

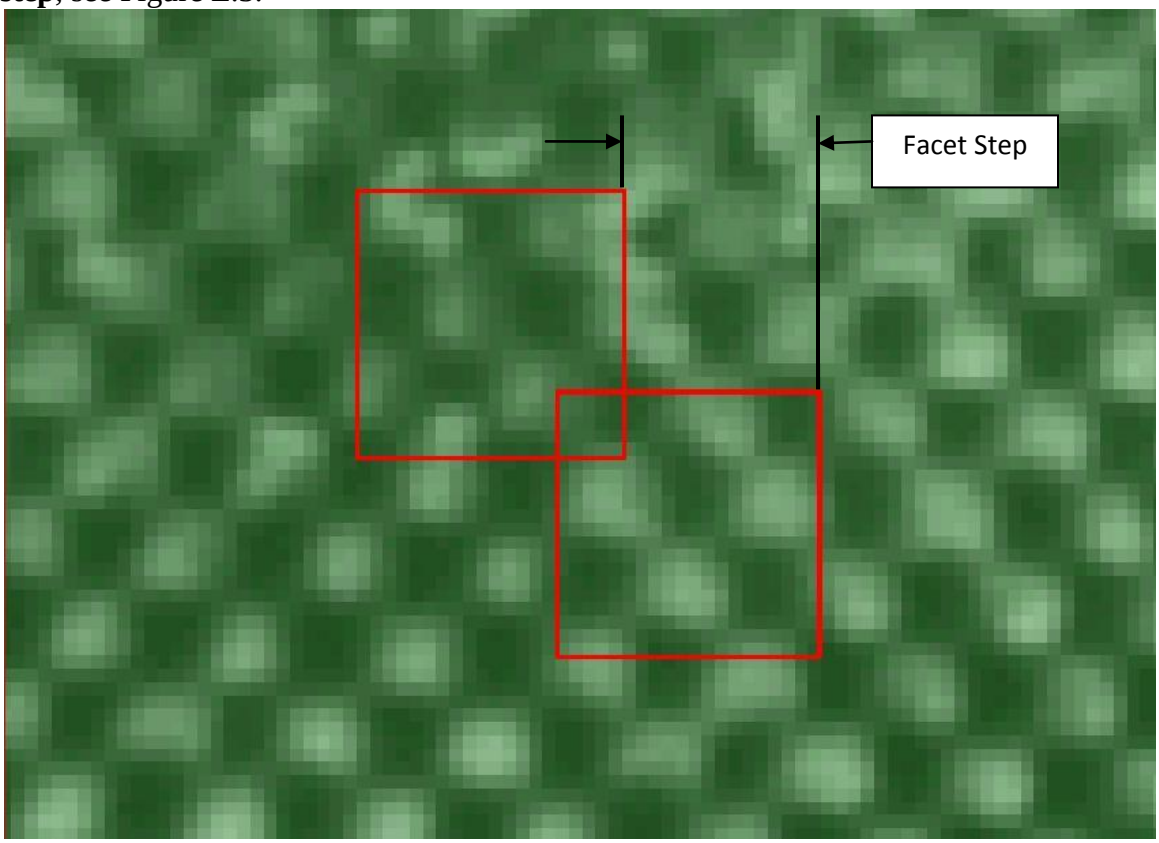

Figure E.3 Illustration of a typical facet step (for a facet that is 20 x 20 pixels).

This facet step determines the spatial resolution between each facet center point on the 3D surface. Once this field of facets is defined, the calculations can be performed by the software and displacement measurements can be viewed. The output is a 3D point cloud, which identifies the position of all the facets within any given stage. As the surface of the structure changes from one stage to the next, the geometrical coordinates of each facet will change accordingly. To determine strain from the defined 3D point cloud, several other parameters, computation size and validity quote, must be defined.

The strain for each 3D point on the measured surface is calculated by measuring the deformation of an array of surrounding points from stage to stage, as shown in Figure E.4. As the array of 3D points deform, the displacement from the original length is calculated for the two-dimensional plane tangential to the measurement surface. Using the finite-strain equations described earlier, the linear strains in each x and y directions are calculated, as well as the shear angle.

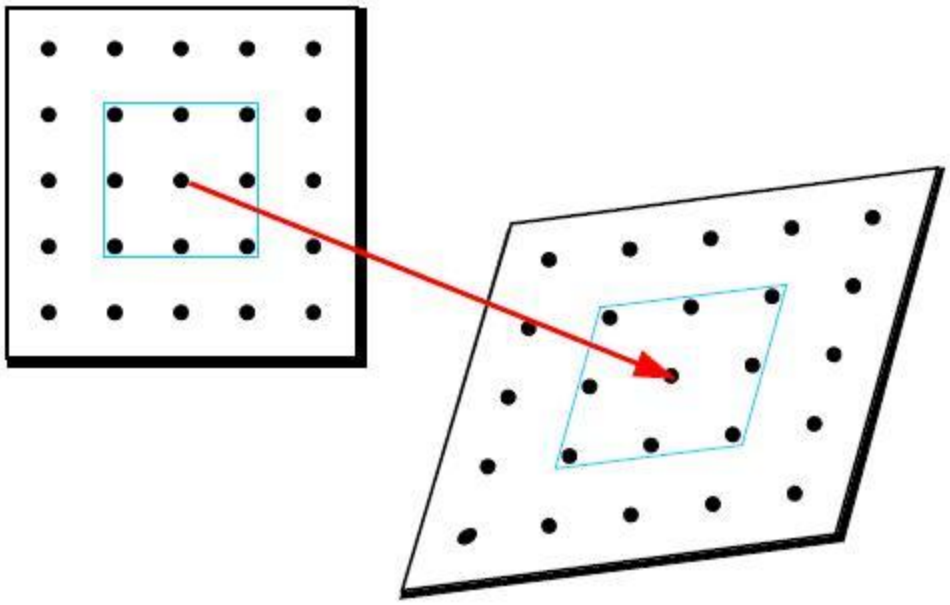

Figure E.4 Strain computation from 3D points (5).

The total deformation of this set of 3D points relative to the defined reference stage defines the amount of strain computed at that center point. The size of surrounding array of points is known as the **computation size** of the project, and essentially establishes the strain-gage length for the project as the linear strains are calculated over this computation size, see blue box (computation size of three) in Figure E.4. The noise floor of the measurement is directly related to the computation size of the project, and the sensitivity to the amount of strain which can be measured decreases as the computation size increases. A **validity quote** is established in the cases where the entire array of surrounding points might not be available, such as on the edge of a surface. This parameter is defined as the percentage of surrounding points that are used in the strain calculation. If the number of 3D points surrounding the point of interest is below this parameter, then the strain will not be calculated for that point. The ARAMIS™ default values are set to a computation size of three and a validity quote of 55% of surrounding points.

1.4 FILTERING

Once a project is computed, and a set of 3D points is defined with all surface deformations calculated, a final step of filtering is usually applied to the data to reduce experimental and computational noise. Typically a median spatial filter is used. The process of filtering involves calculating the median strain (or displacement) value of a matrix of 3D points (e.g. 5x5 or 7x7). The median value obtained from the matrix is assigned to the center point. The filter is applied to each point on the surface of the structure within the field of view. This filtering process can be repeated over all of the facets depending on the measurement and result required. Each time a filter is applied, it is referred to as a "run." The size of the matrix over which the median value is calculated can also be set to a suitable number depending upon the test subject. The default values for an ARAMIS™ strain calculation is a filter size of seven, with a run count of three, (meaning that a matrix of 7x7 points was used in the median filter, and the filter was applied three successive times). For a displacement calculation it is suggested to use a size of five and run count of two. The settings used for all DIC measurements included in this project are described in Table B-1.

Table B-1 Parameter settings for Aramis calculations.

Parameter	Displacement	Strain
Facet Size	20	20
Facet Step	15	15
Computation Size	-	5
Filter Size	5	7
Filter Runs	2	3

1.5 PRELIMINARY TEST ON CX-100

Before testing the blade with embedded defects, it was important to perform a preliminary test on another CX-100 blade to identify an appropriate testing methodology. This testing was performed at the NREL National Wind Technology Center (NWTC) in Boulder, CO. The test article was mounted to a large steel test stand, which is used to cantilever the blade for both static and fatigue loading (6; 7). Prior to DIC inspections, the blade was subjected to a fatigue test to demonstrate the durability of the blade and a specialized Sandia National Laboratories instrumentation package (8; 9).

During the fatigue test, two damage areas were observed and tracked as the damage developed throughout the testing. Damage areas include along the trailing edge of the blade and on the low-pressure skin at approximately 1 meter span from the root of the blade. Both damage areas were between the root and maximum chord of the blade, with the span location represented by the large red box as shown in Figure E.5. The DIC measurements of full-field displacement and strain were performed on this area. The smaller blue box located at a span of approximately 6.75 meters (as shown in Figure E.5) indicates the area of the static loading applied during the testing.

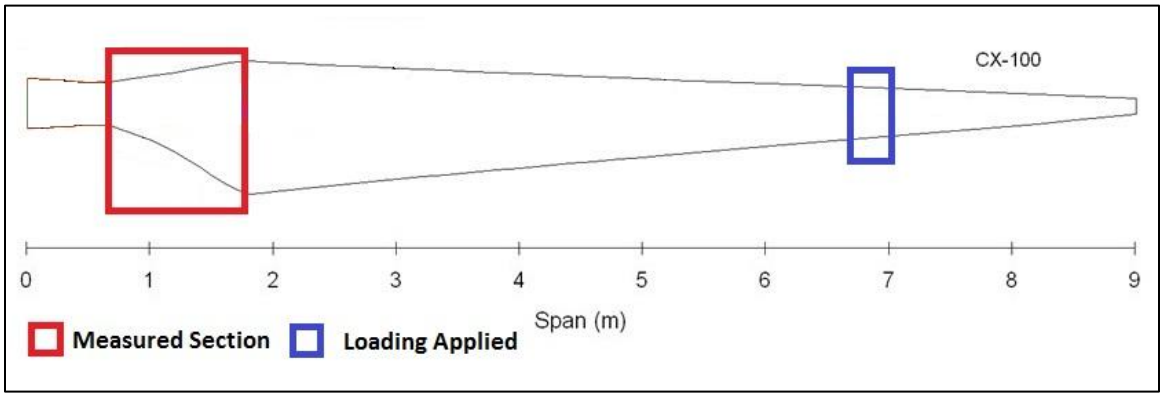

Figure E.5 Planform view of the CX-100 wind turbine blade, indicating the DIC measurement and loading locations.

Prior to collecting data, the surface of the blade was sanded to remove the glossy gel-coat and a random speckle pattern was applied using permanent-ink markers. For the high-pressure surface (HPS) test, the cameras were mounted to a gantry straddling the blade to provide the

required field of view. Three 1000-watt studio lights were used to light the area of interest sufficiently. The test setup with blade, saddle, and applied load (via suspended dead weights) is shown in Figure E.6.

.

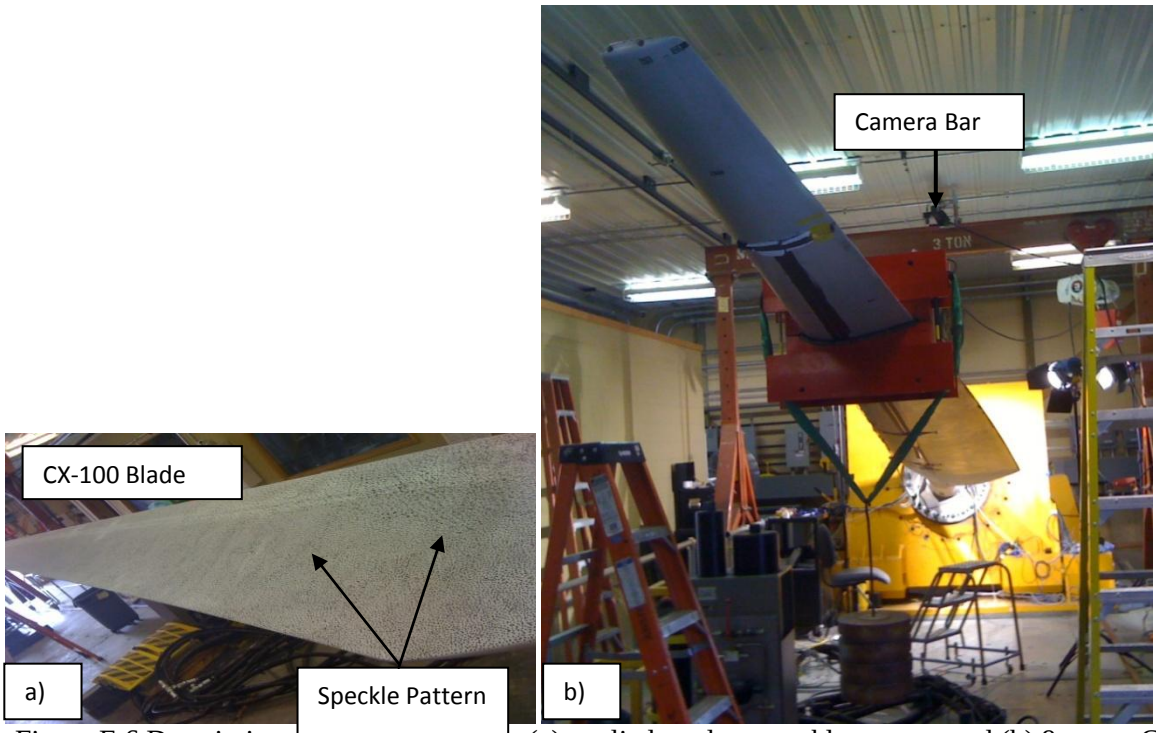

Figure E.6 Description of [illegible]: (a) applied random speckle pattern, and (b) 9-meter CX-100 blade mounted to the test stand with applied load hanging from saddle. The camera bar is mounted to the gantry, and studio lights are in position.

Data were collected in the specified area on the HPS, the low-pressure surface (LPS), and trailing edge of the blade while unloaded and using a stepped loading of 50-lb increments from 150 to 400 lb. A series of five images was taken at each loading level. The locations of the cameras and lights were adjusted depending on which section of the blade (HPS, LPS, or trailing edge) was being tested. Again note the blade had undergone fatigue testing prior to these DIC tests, and had well-developed damage areas in the measured section between the blade root and the maximum chord location.

1.6 TEST OF DEFECT FREE LOS ALAMOS BLADE

The defect free blade owned by Los Alamos National Labs (LANL) is used as the control to which the defect blade is compared to. Therefore baseline DIC measurements were performed on each of the locations where defects were embedded. An approximately one meter field of view surrounding the 3.5, 5, and 6 meter locations was prepared for testing by first lightly sanding off the gel coat, applying a coat of flat white spray paint and finally using a pattern to spray the required stochastic dot pattern onto the blade surface.

Figure E.7 shows the LANL blade with required locations prepared for DIC measurement. As shown in Figure E.7 saddles were mounted to the blade. These saddles were to provide the required excitation for the scheduled fatigue test.

Figure E.7 LANL defect free blade with DIC patterning.

The 3D DIC system cameras were first calibrated for a 1 meter field of view, and then mounted to an overhead gantry as shown in Figure E.8. Once mounted to this gantry, three 1000 watt spotlights were used to light the required field of view. A large dead weight of 520 lb was hung from the outboard saddle at a span position of 6.75 meters as shown in Figure E.9. A series of five image stages were taken, at a rate of 12 Hz, in both unloaded and loaded states. This test methodology was repeated for each measurement location.

Figure E.8 Camera bar mounted to overhead gantry.

Figure E.9 LANL CX-100 nine meter blade under load.

1.7 PRELIMINARY CX-100 TEST

Measurements were first made on the HPS of the CX-100 blade surface. The full-field curvature of the blade as a function of both load and section length is shown in Figure E.10. The processed data is used to show the displacement and curvature of the blade as a function of the

various loading levels. To gain further insight into how the blade was affected by the previously conducted fatigue testing, the full-field strain contour over the blade surface was analyzed. The results are shown in Figure E.11. There is a localized high level of strain at approximately 700 mm from the left portion of the image. This result indicates that something is causing this strain amplification in the observed section of the blade.

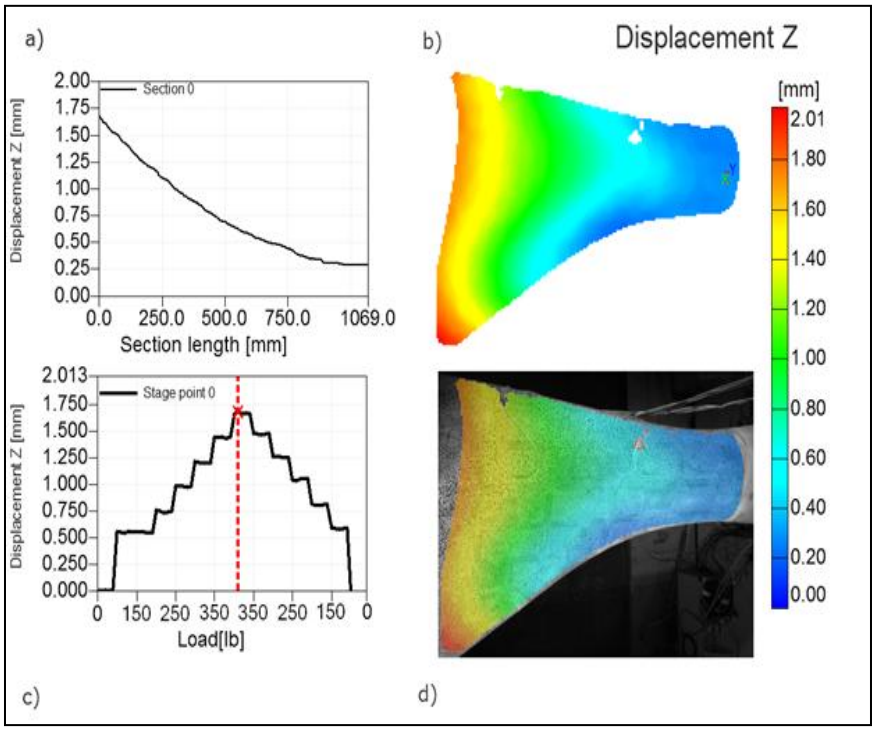

Figure E.10 Measurement displaying curvature of blade along the HPS at a 400-lb load level (a) displacement section line along the length of the blade (root shown on right); (b) spatial displacement contour near the blade root; (c) displacement along the left side

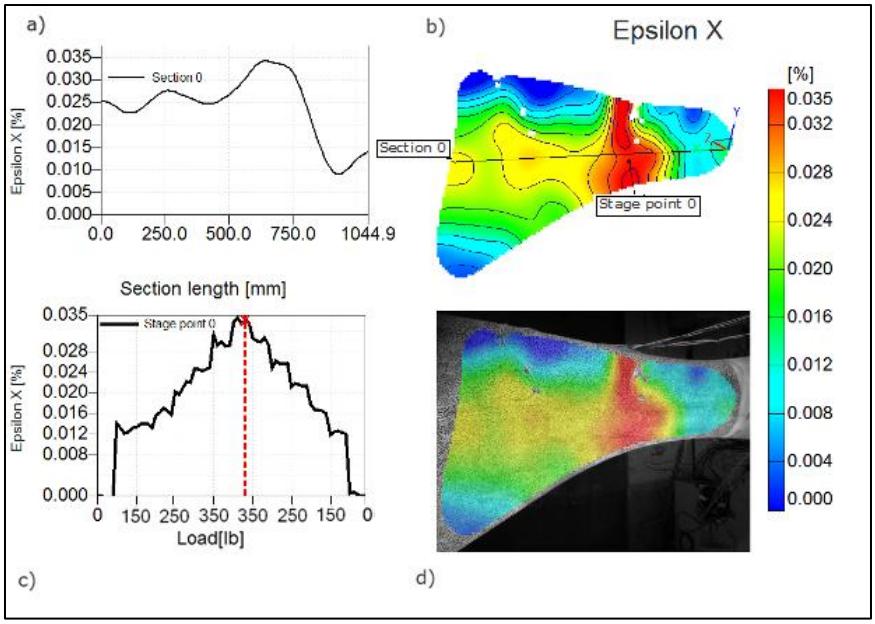

Figure E.11 Measurement displaying strain of blade along HPS at a 400-lb load level (a) strain along section line lengthwise of blade (root shown on right); (b) spatial strain contour near blade root; (c) strain at point 0 (shown in (b)) as a function of applied load

When the LPS of the blade was tested in the same manner, a discontinuity in curvature was observed, as shown in Figure E.12(a). A visual inspection indentified a large crack in the blade at the location of the measured discontinuity. The corresponding displacement contours shown in Figure E.12(b) and Figure E.12(d) also reveal a spatial displacement discontinuity in the blade. When the displacement at locations on opposite sides of the crack are compared, the displacement at the location near the blade root (point 1) no longer is being loaded in the same manner as the displacement locations between the crack and the applied load (see Figure E.12(c)). This loading difference implies that the load path has been changed due to the presence of the crack. The presence of the crack or damage location is even more revealing when the strain field is observed, as shown in Figure E.13.

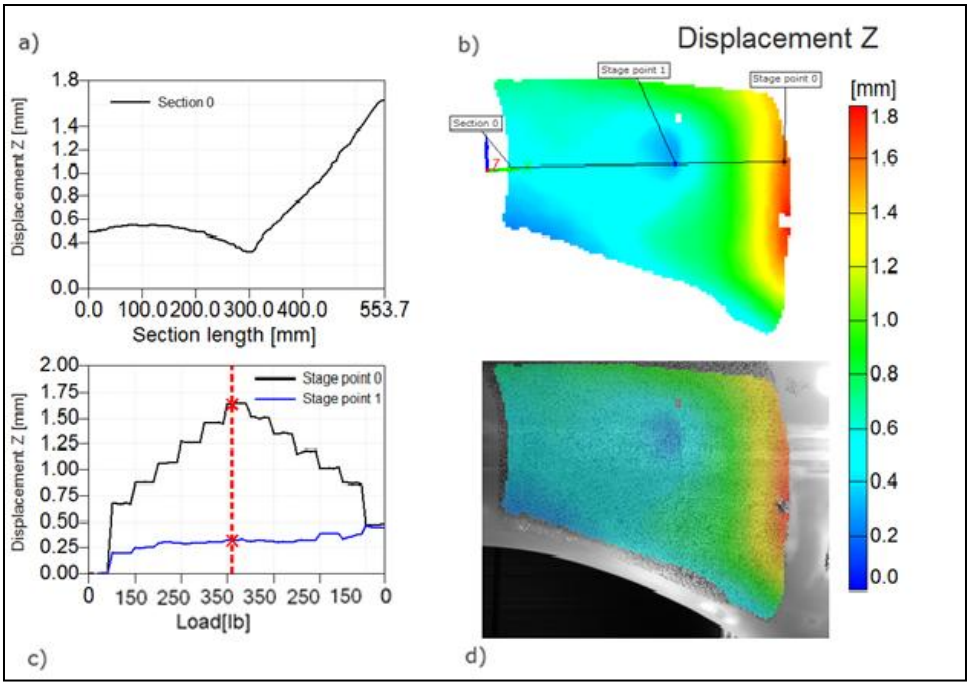

Figure E.12 Measurement displaying blade curvature along LPS at a 400-lb load level (a) blade curvature along section line lengthwise of blade (root shown on left); (b) displacement contour near blade root; (c) displacement at points 0 and 1 (shown in (b)) as a function of applied load; and (d) overlay of displacement contour with blade image.

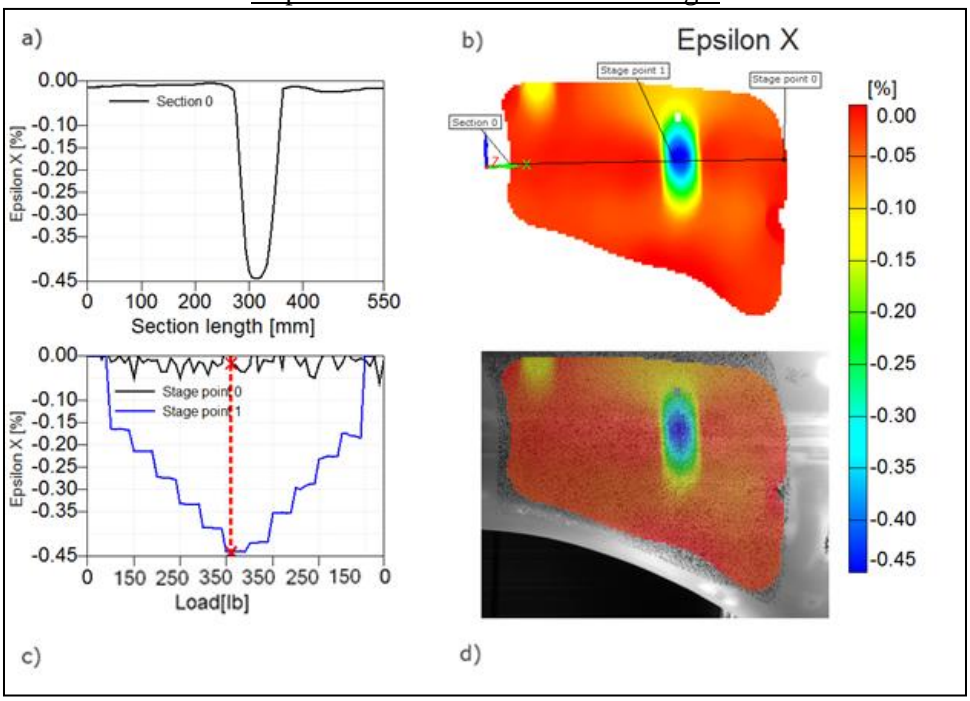

Figure E.13 Measurement displaying strain of blade along LPS at 400-lb load level (a) strain along section line lengthwise of blade (root shown on left); (b) spatial strain contour near blade root; (c) linear elastic strain as a function of load at points 0 and 1 specified in (b); and (d) overlay of strain contour with blade image.

The section line of Figure E.13(a) shows an amplification of strain in the location of the damaged area. The contour shown in Figure E.13(b) indicates that there is a crack or "damage" causing a locally high strain in the area. This crack is approximately co-located on the opposite surface of the high strain witnessed in the HPS test. The strain is negative in the LPS tests due to a compressive load, whereas the positive strain in the HPS test is due to the tensile load on the high-pressure skin of the turbine blade during these tests.

During the fatigue loading of the blade a second significant damage area along the trailing edge of the blade was observed. The same stepped loading cycle as previously described was applied when measuring this portion of the blade. The strain results for the trailing edge are shown in Figure E.144.

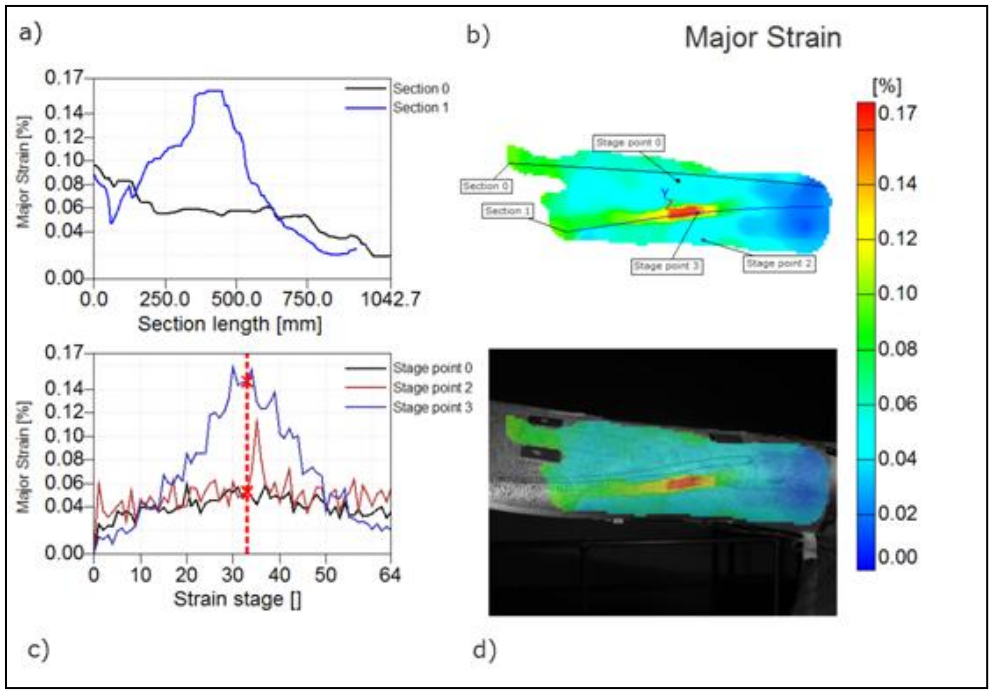

Figure E.14 Measurement displaying major strain of blade along trailing edge at a 400-lb load (a) comparative strain along section lines 0 and 1 (root shown on right); (b) strain contour near blade root; (c) linear elastic strain at indicated stage points in (b); and (d) overlay of strain contour and blade image.

Major strain is defined as the maximum principle strain occurring at each measurement point on the surface, and therefore is always positive. The major strain contour shown in Figure E.14(d) clearly shows an amplification of strain in the location of a damage area which initiated and propagated during the fatigue testing.

1.8 DATA STITCHING OF PRELIMINARY CX-100 BLADE

The entire surface of the CX-100 blade was captured in loaded and unloaded states with 16 separate fields of view. These separate fields of view were combined, with the use of reference points, to measure full field blade deformations as described in Section 2.5. The technique was first performed within a MATLAB script. A planform view of the three-dimensional stitched blade surface is shown in Figure E.15.

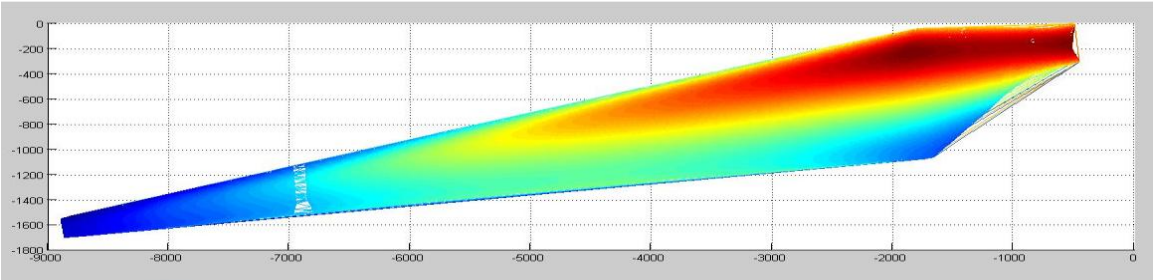

Figure E.15 Planform view of stitched CX-100 9 meter blade surface.

The blade surface was measured in two states, once completely unloaded, and once more with a weight of 350 lb suspended from the 6.75 meter span location. Figure E.16 shows the two measured surfaces overlaid.

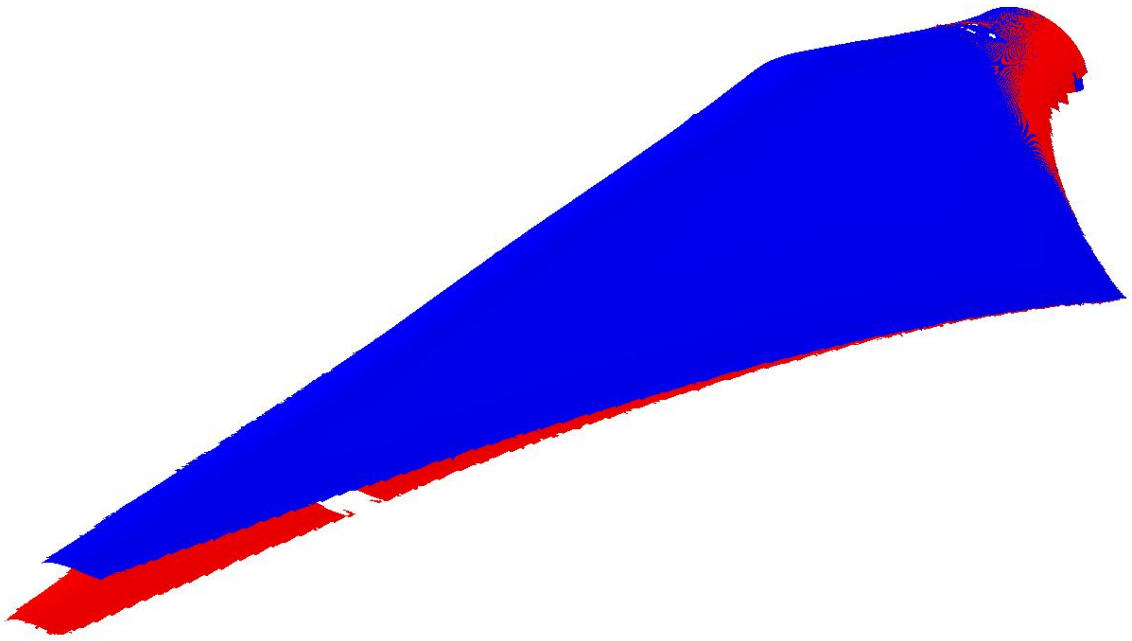

Figure E.16 Overlay of loaded (350 lb, in red) and unloaded (blue) blade surfaces.

The missing data on the loaded blade surface is due to the straps, from which the weights were suspended, covering the DIC patterned surface. The full field displacement from unloaded to loaded states is shown in Figure E.17. The curvature of the centerline of the blade with respect to span location is shown in Figure E.18.

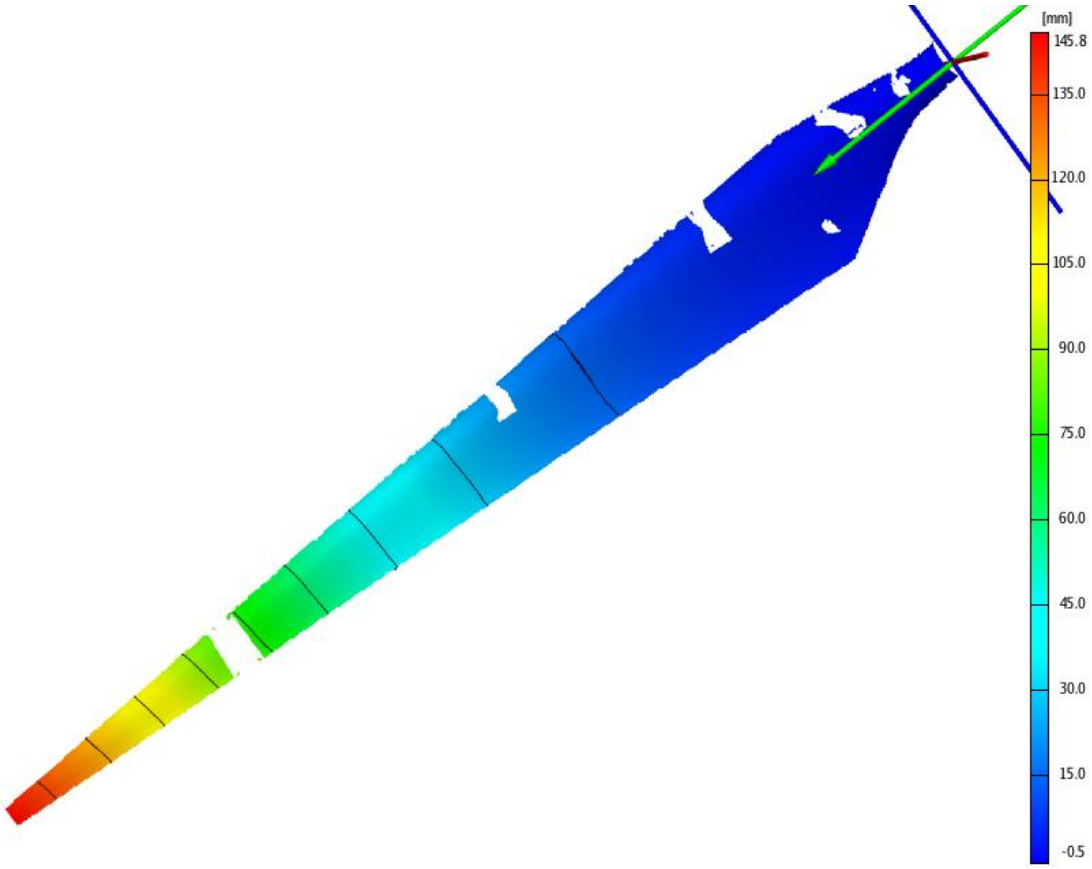

Figure E.17 Blade surface shown with displacement gradient at applied load of 350 lb.

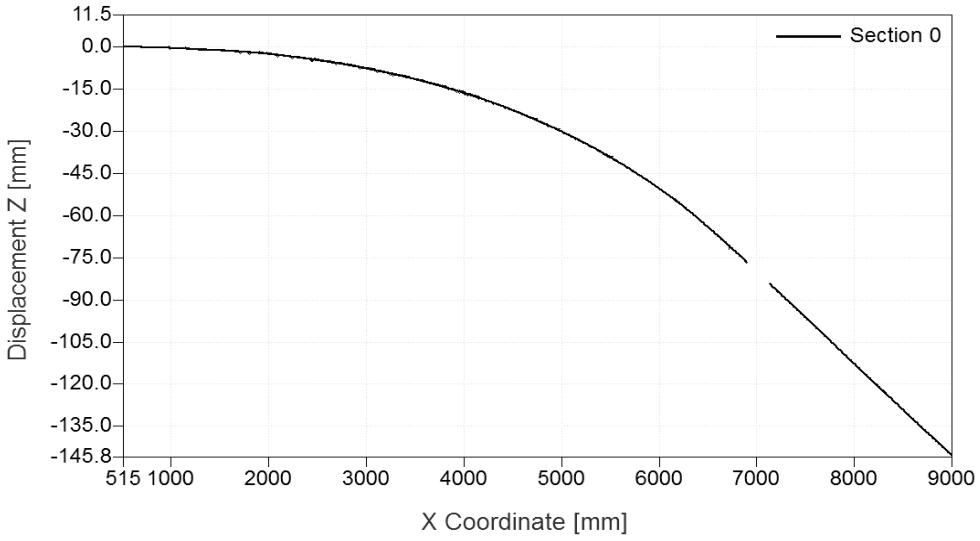

Figure E.18 Blade centerline curvature vs. blade span location with applied load of 350 lb.

The measurement recorded a 146 mm tip displacement for the 350 lb load applied at the 7 meter span location. As shown in Figure E.18, the curvature from one measured field of view to the next is continuous showing no observable degradation due to stitching. However, a study

should be performed comparing the added error in each additional stitched surface to the amount of reference points used in the stitching process.

The span-wise strain overlaid on the CX-100 surface for the same loading situation is shown in Figure E.19. Span-wise strain as a function of span location is shown in Figure E.20. Areas of measurement dropout in Figure E.19 are due to other instrumentation covering the blade surface. Therefore an accurate measurement could not be made in these areas. Several observations that can be made from the strain distribution on the HP surface of the blade is the concentration of high strain areas toward the leading edge of the blade on the spar cap. This is to be expected as the shear web, which bridges the HP and LP surfaces of the blade, mounts to this spar cap. The area of highest strain due to the loading scenario, also observable in Figure E.20, is located just past the 5 meter location. Also, notice the area close to the root of the blade also contains an area of high strain, which was witnessed in the close up testing of the preliminary blade and showed in detail Figure E.11.

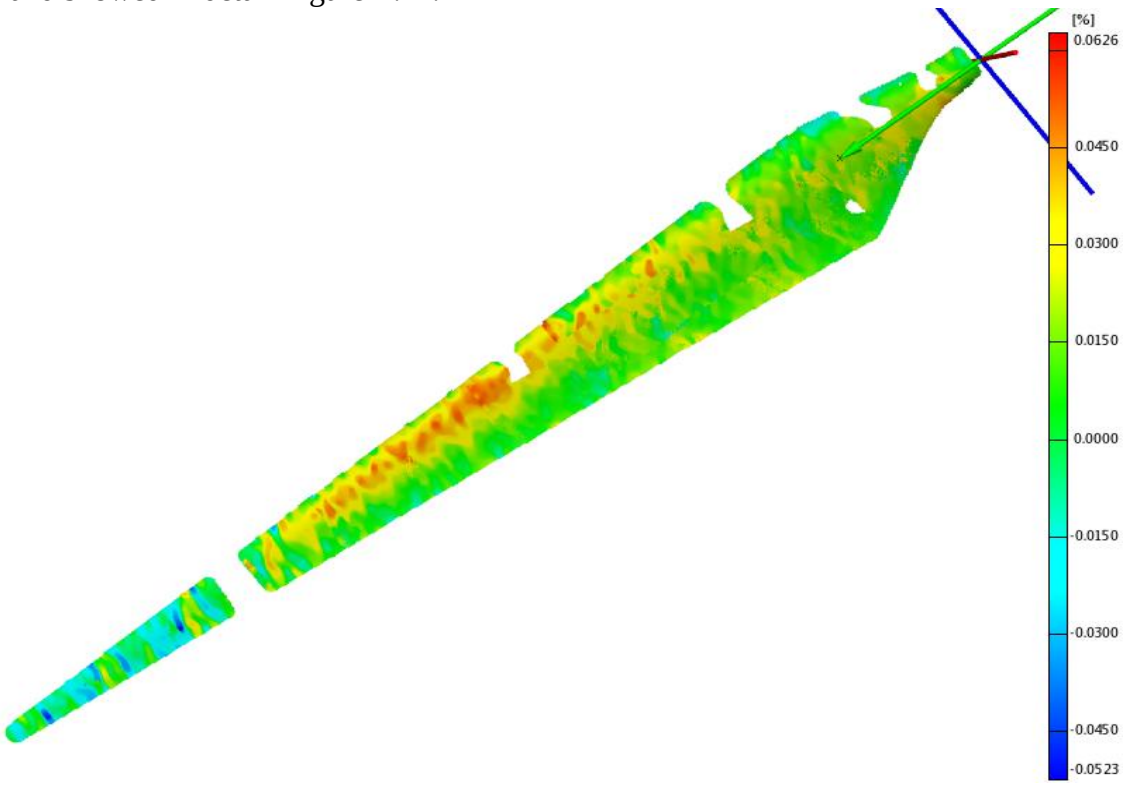

Figure E.19 Blade surface shown with calculated distributed strain for an applied load of 350 lb.

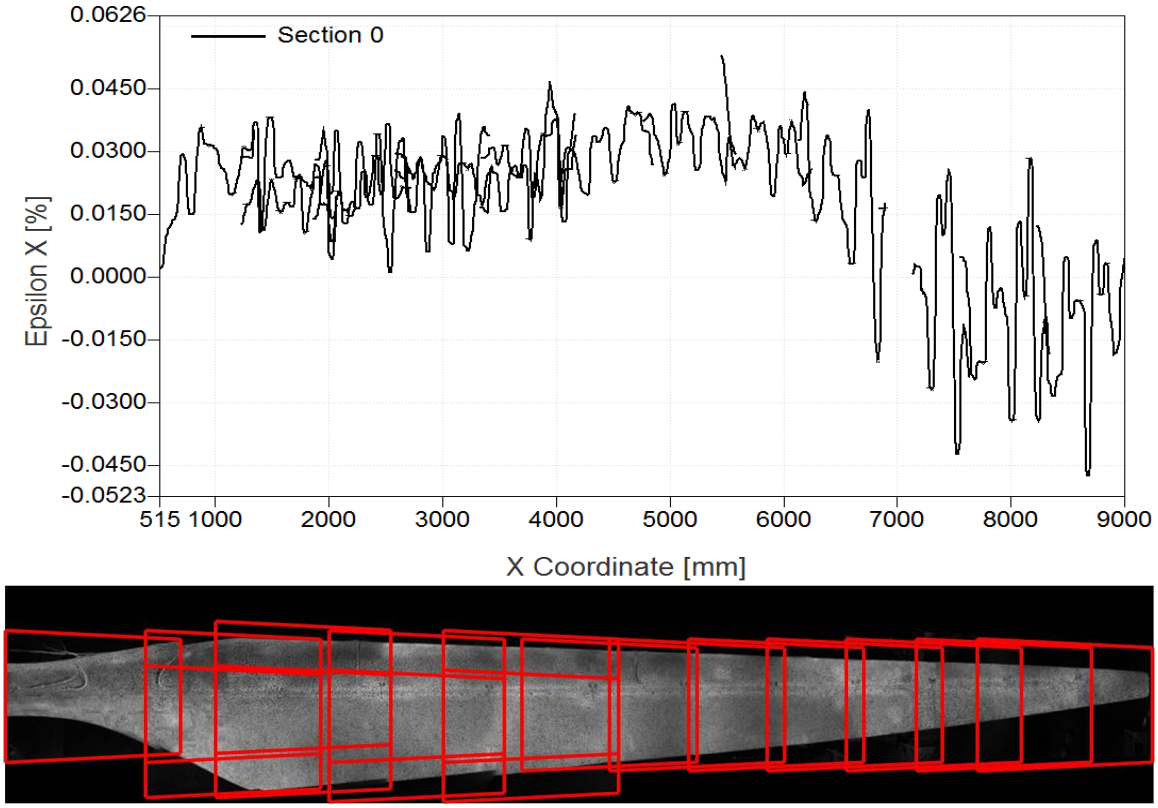

Figure E.20 Span wise strain along the centerline across the length of the blade for an applied load of 350 lb.

The strain displayed in Figure E.20 shows overlapping curves. Each line represents an individual section, i.e. a measured field of view. There are 16 separate curves, each approximately a one-meter section along the length of the blade. The separate curves show the overlapping sections. Each section's strain is filtered within its own field of view. Therefore when overlapped with the next strain surface, the filtering is slightly different, which results in small deviations of strain measurement. The same is true for the displacement graph, shown in Figure E.18. However the noise on the displacement measurement is smaller than the actual width of the curves, so the curves appear as a single trace.

The strain measured throughout the full length of the blade shows the highest strain due to the applied load at approximately the 5 meter span location. The strain measured in the prior stepped loading tests showed a spike in strain at approximately the .75 meter span location. The result is also visible in Figure E.19. However the strain measured at the 5 meter location, in the area of the spar cap, is greatest.

Having gained knowledge of the strain distribution across the HPS of the blade in a static loading scenario, the tests to identify the strain amplification due to the manufactured defects can begin. The defect free LANL blade was tested as a baseline in which to compare the future results of the UMass Lowell blade with embedded defects.

1.9 LOS ALAMOS DEFECT FREE BLADE

The Los Alamos National Laboratory (LANL) CX-100 blade was manufactured in a similar manner to the UMass Lowell blade, but without any of the custom made defects present. Therefore the LANL blade is used as a baseline defect free blade with which to compare the behavior of the CX-100 blade with defects.

The blade was loaded at the 6.75 meter span location with a 520 lb weight, as previously described. The locations that correspond to each region of interest, 3.5, 5, and 6 m, where the defects are present in the UMass Lowell blade, were imaged in a loaded and unloaded state. Testing of the LANL blade was performed twice during the fatigue loading of the blade. A set of data was taken, as a baseline, without any significant number of loading cycles applied, and once again at a cycle count of 955,220. The following outlines the displacement and strain comparisons for each measured section between baseline and 955,220 cycles. Figure E.21 and Figure E.22 display the strain distribution centered on the 3.5 meter HPS area for the baseline and after 955,220 cycles, respectively.

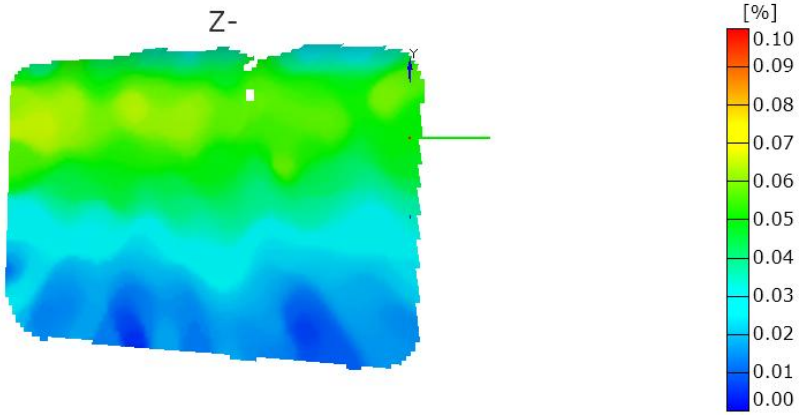

Figure E.21 Baseline Strain field at the 3.5 meter span location on the high pressure surface loaded to 520 lbs.

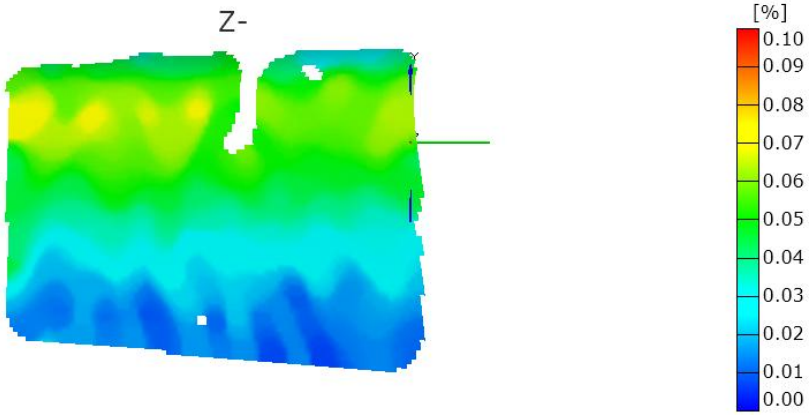

Figure E.22 Strain field at the 3.5 meter span location on the high pressure surface loaded to 520 lbs after 955,220 cycles.

As shown in the above figures, the areas of highest strain are concentrated around the top of the image. This area of high strain corresponds with the location of the spar cap and shear web within the blade. After loading for over 955,000 cycles, there are slight variations in the measured strain, as depicted by the increased amount of yellow in the images. However, very

little overall strain differences were measured between the two tests. Reference points were placed on the blade, prior to loading, in each measured section to give a direct comparison of strain across a section line, see Figure E.23. This referencing process was performed in each test section.

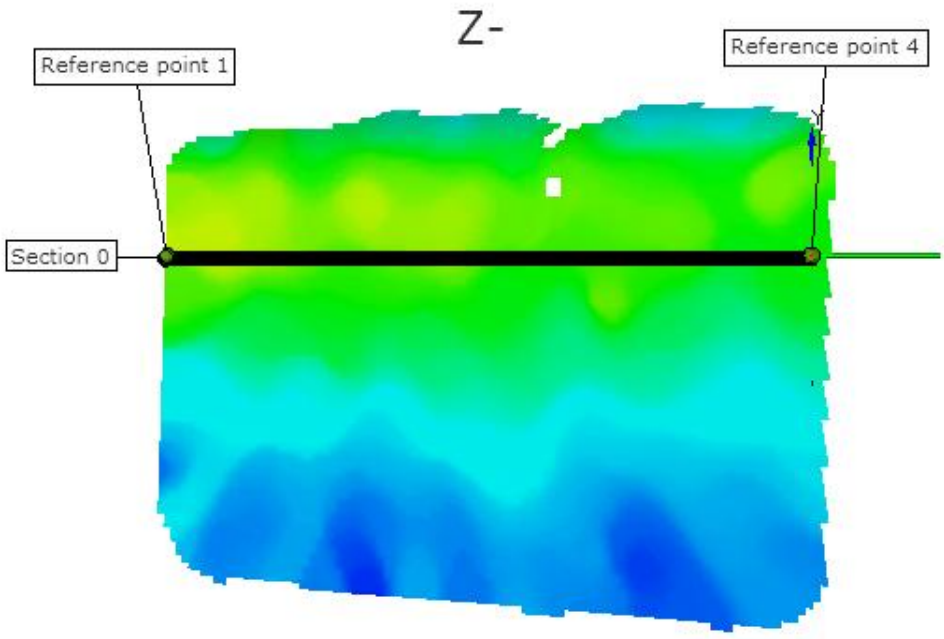

Figure E.23 Definition of section and reference points for each position measured.

A comparison, between baseline and after 955,220 cycles, of the strain and displacement over "Section 0", defined in Figure E.23, is shown in Figure E.24 and Figure E.25, respectively.

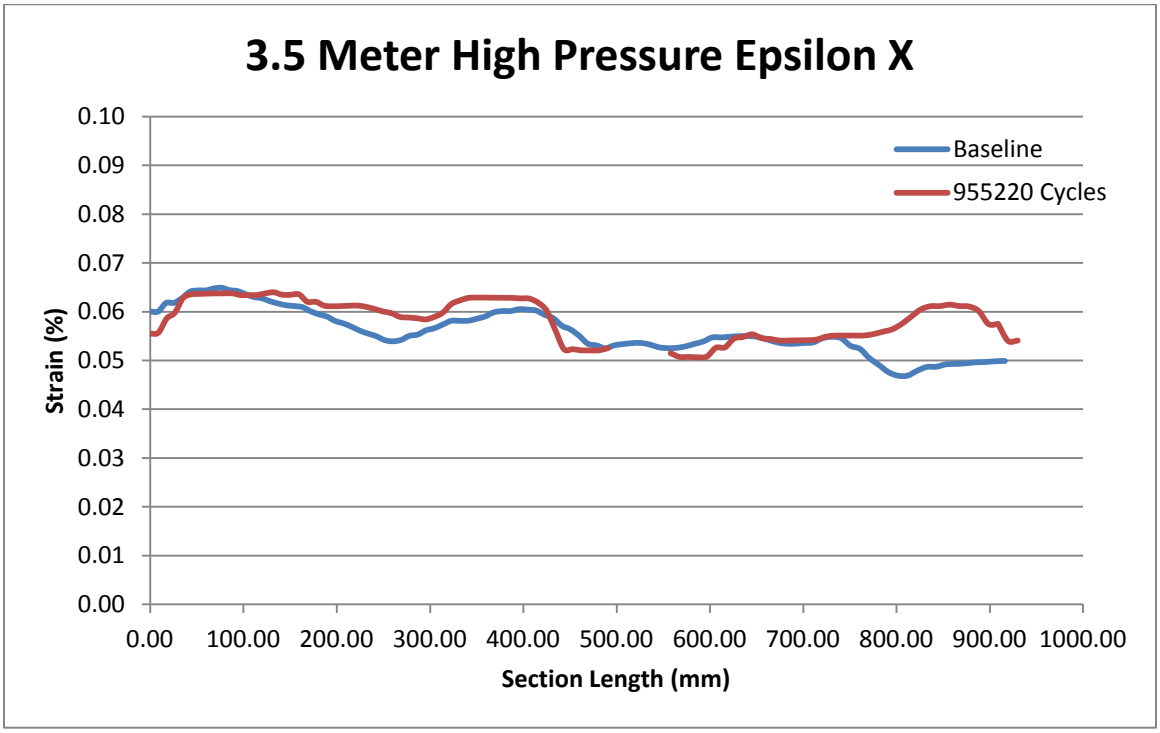

Figure E.24 Strain comparison between baseline and 955,220 cycles at 3.5 meter location.

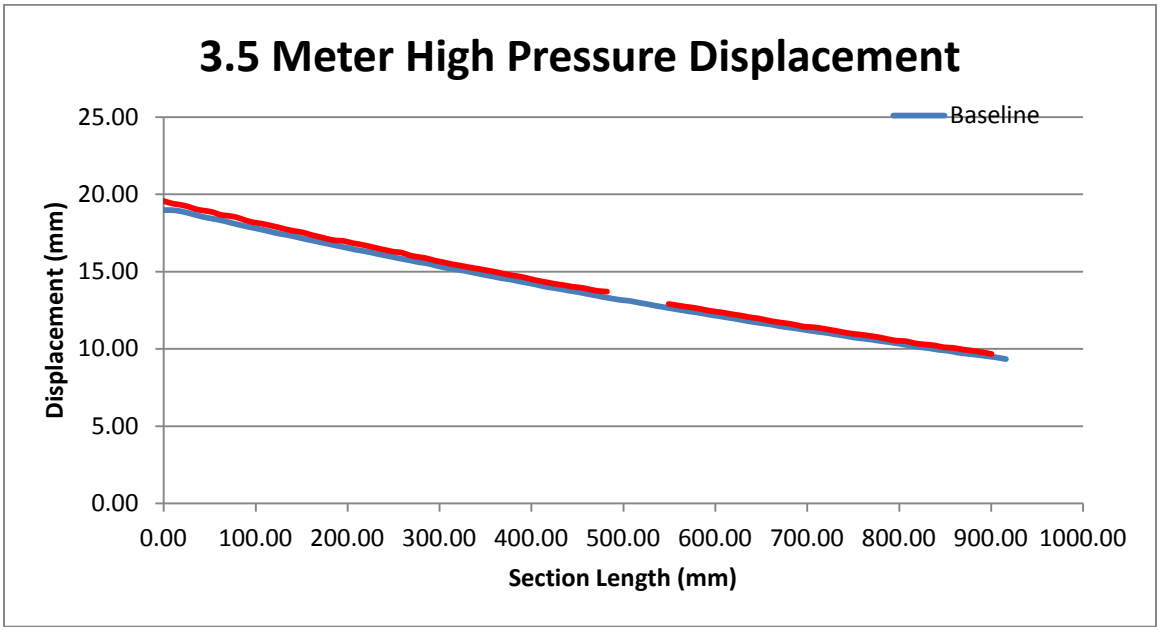

Figure E.25 Displacement comparison between baseline and 955,220 cycles at 3.5 meter location.

The measured strain in Figure E.24 shows the small differences between the two tests. The strain is slightly higher along the section length after the ~955,000 cycles are applied although there are no significant changes in the blade surface characteristics. The displacement shown in Figure E.25 shows slightly more displacement (0.59mm), after the cycling than that of the baseline measurement at the 3.5 meter location. However the curvature remains fairly constant. The results at the 5 meter location, shown in Figure E.26 through Figure E.29, appear to be similar. Any dropouts in data are due to other sensors installed in the area, along with cabling, which prevented measurement on the surface of the blade.

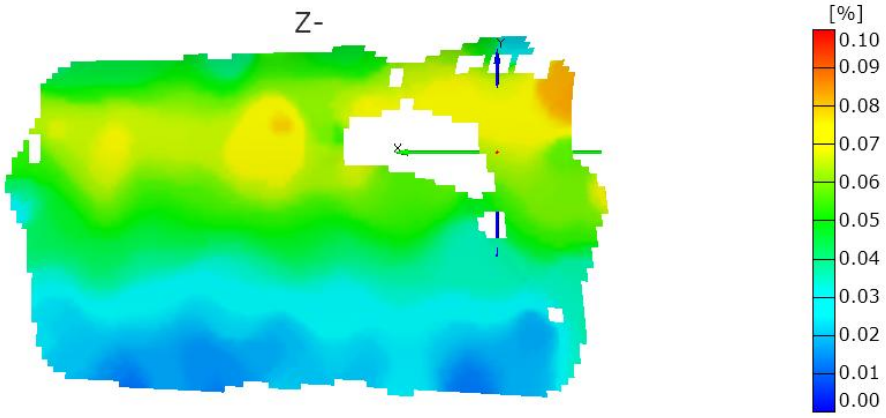

Figure E.26 Baseline Strain field at the 5.0 meter span location on the high pressure surface loaded to 520 lbs.

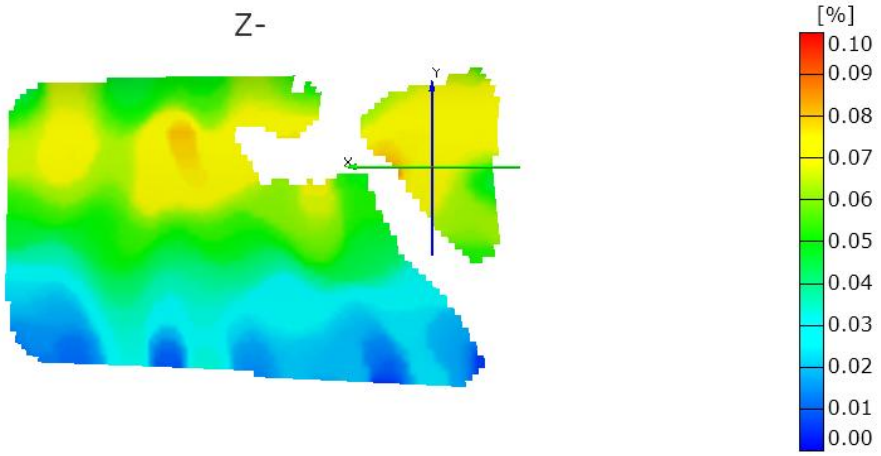

Figure E.27 Strain field at the 5.0 meter span location on the high pressure surface loaded to 520 lbs after 955,220 cycles.

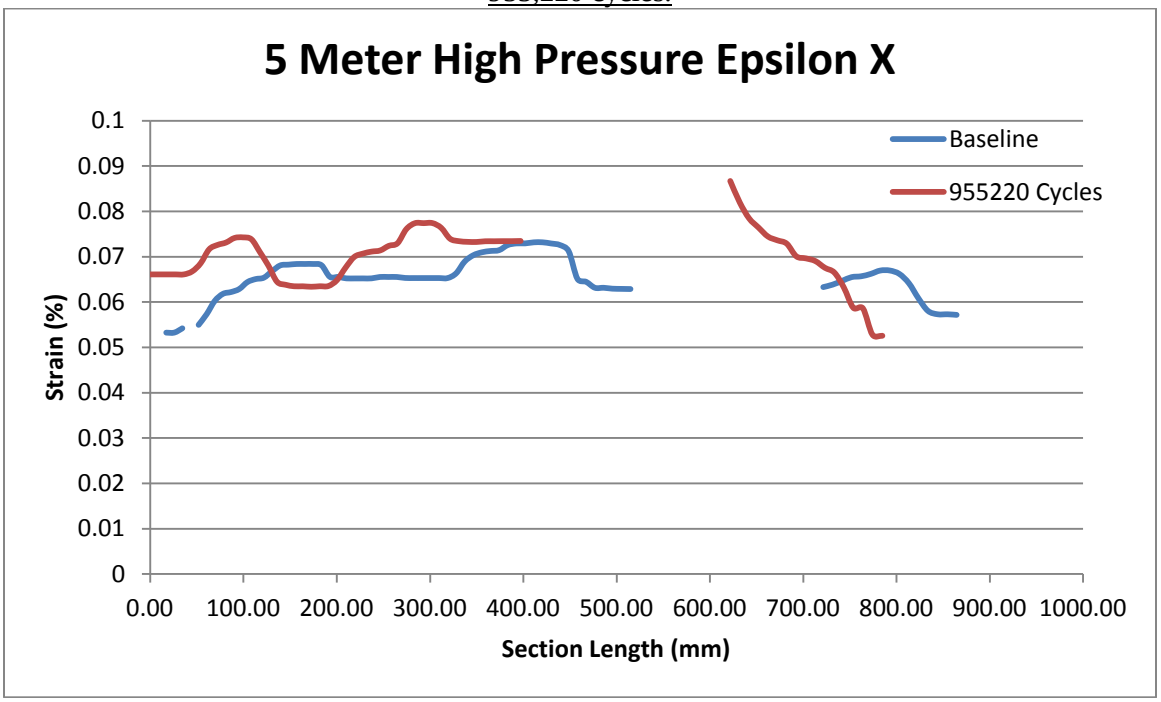

Figure E.28 Strain comparison between baseline and 955,220 cycles at 5 meter location.

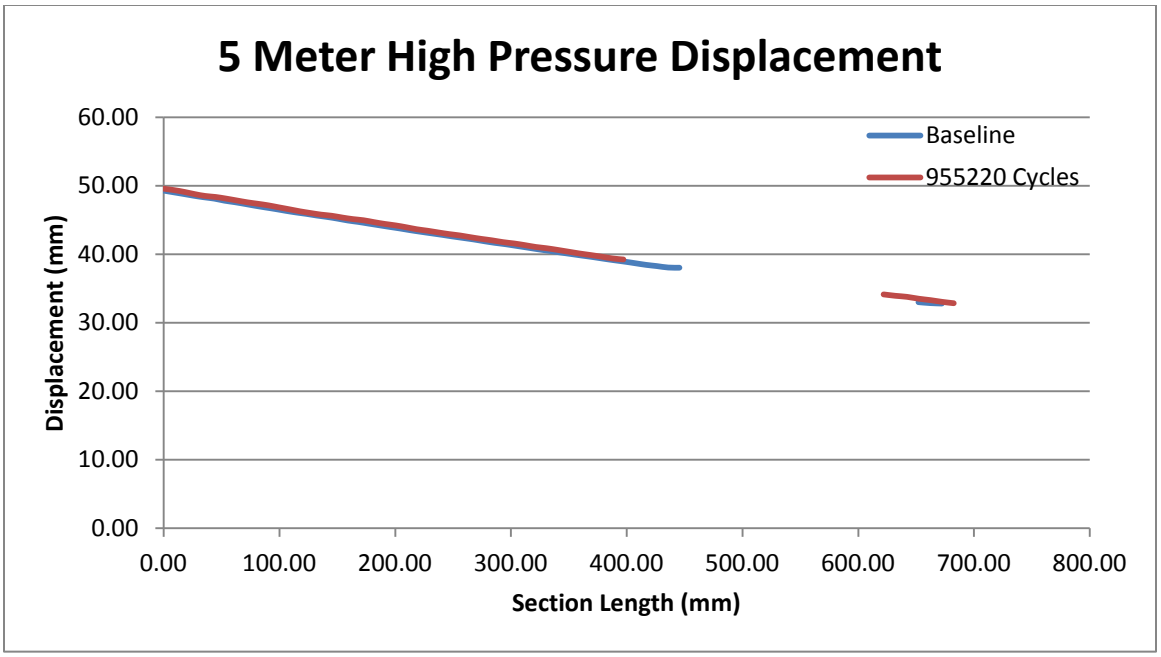

Figure E.29 Displacement comparison between baseline and 955,220 cycles. at 5 meter location.

The data from the 5 meter section of the blade exhibits similar behavior at 955,220 cycles as at the baseline. The strain field is slightly more erratic with higher amplitude peaks at 955,220 cycles, although the curvature of the blade remained constant after the fatigue loading cycles. The data collected for the 6 meter section, shown in Figure E.30 through Figure E.33, is consistent with the other measured sections.

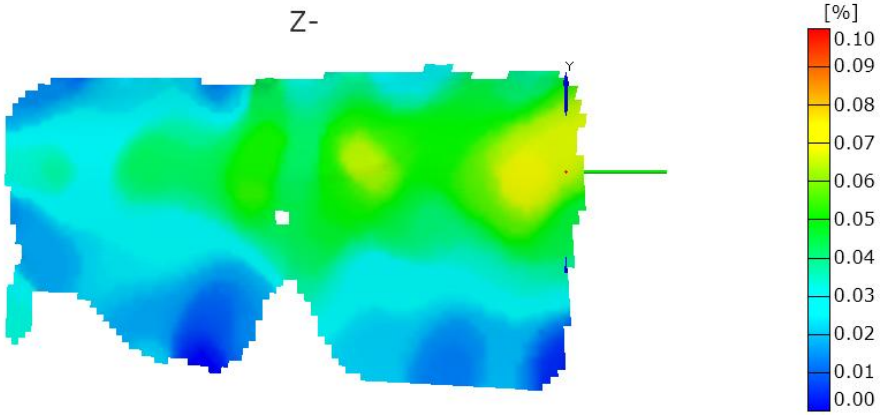

Figure E.30 Baseline Strain field at the 6.0 meter span location on the high pressure surface loaded to 520 lbs.

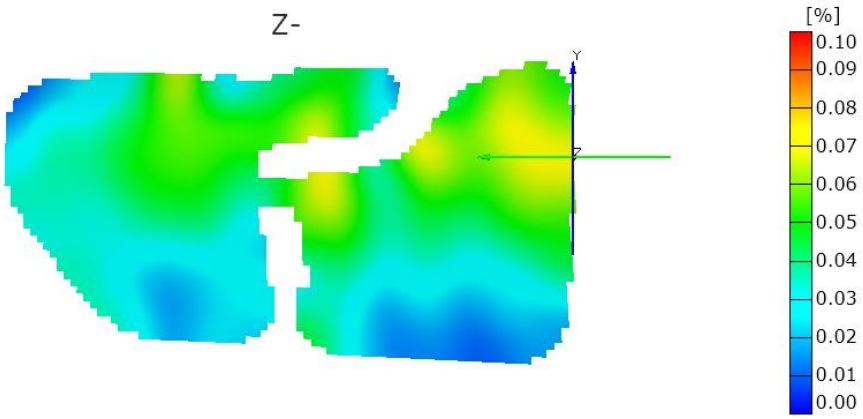

Figure E.31 Strain field at the 6.0 meter span location on the high pressure surface loaded to 520 lbs after 955,220 cycles.

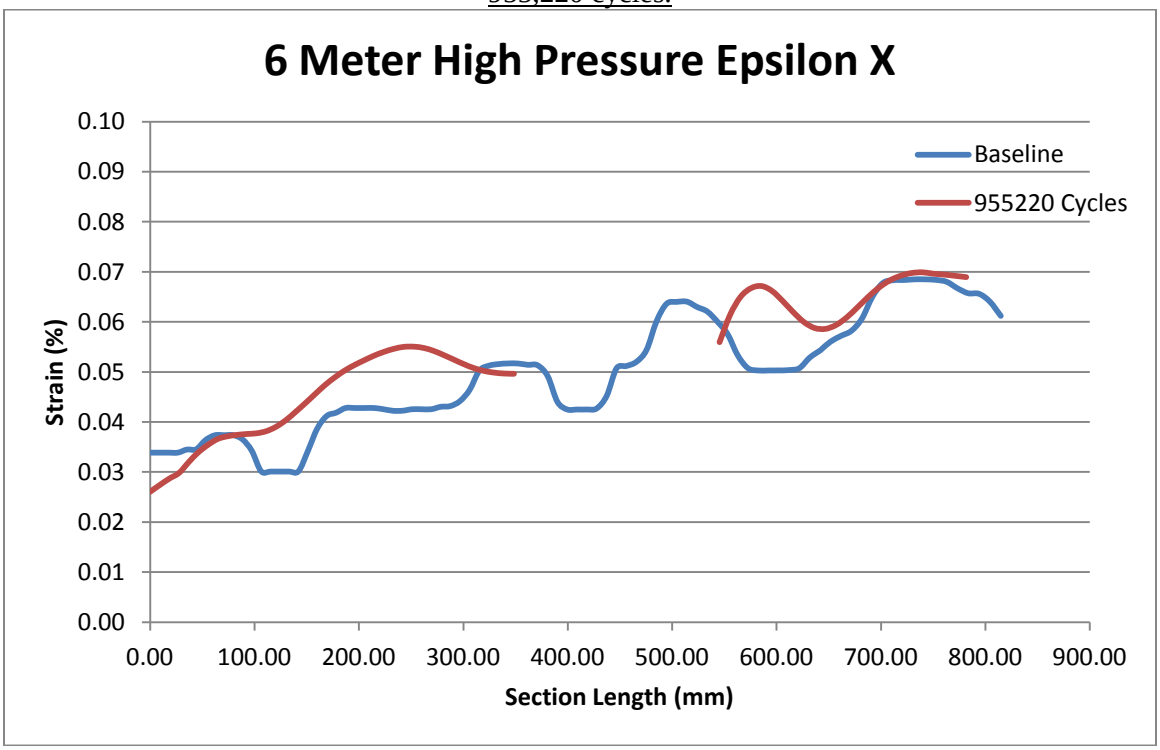

Figure E.32 Strain comparison between baseline and 955,220 cycles at 6 meter location.

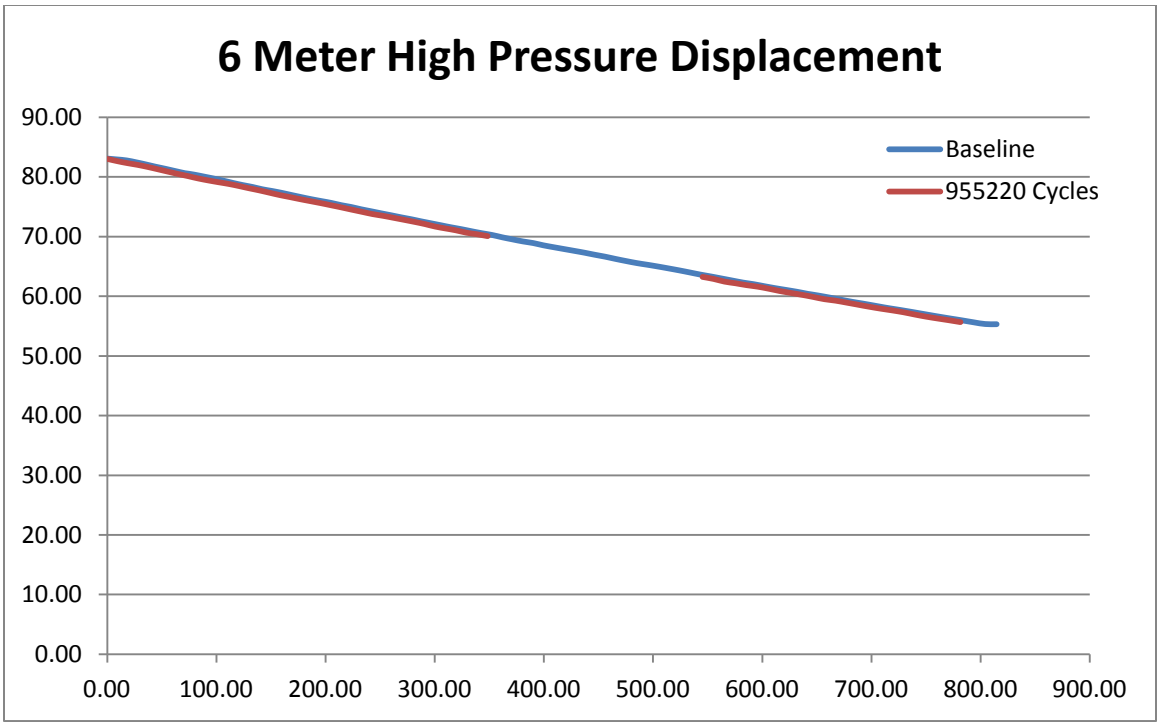

Figure E.33 Displacement comparison between baseline and 955,220 cycles at 6 meter location.

The strain across the surface of each section presented showed similar patterns to those measured in the previous full blade test. Strain is highest in the 5.0 meter section along the spar cap with a peak strain of approximately 0.08 %. The results for the low pressure surface are shown in Table B-2.

As seen in each measured section of Table B-2 the calibration and field of view was not consistent between each test, which results in slightly different measurement volumes and different shaped sections. However each field of view was centered on the defect location, so the measured fields are comparable. Each LPS section displayed in Table B-2 exhibits similar behavior to those measured on the HPS, with the compressive strain levels slightly increased in the higher cycle test. The LPS of the blade was difficult to measure due to setup limitations (cameras on ground with a much smaller field of view and awkward positioning) resulting in a higher noise floor of approximately of .014 % , or 140 microstrain. Any drop outs in data were due to other instrumentation and cabling preventing measurement on the blade surface.

The results presented on the LANL blade are used as a baseline for testing of the UMass Lowell blade which contains defects centered at the locations measured.

Table B-2 Low pressure surface epsilon x comparison.

	Baseline	955,220 Cycles
3.5m	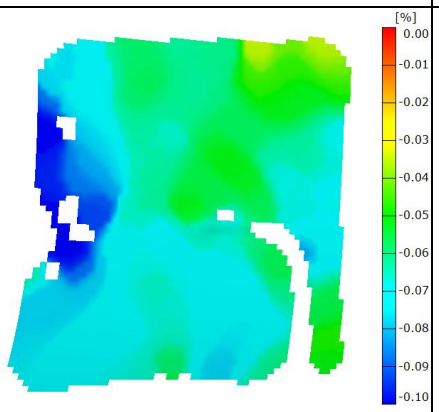	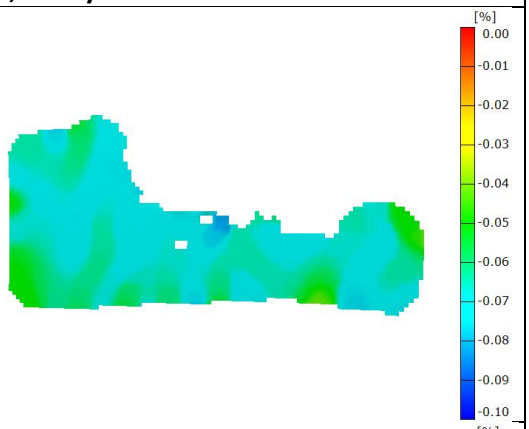
5.0m	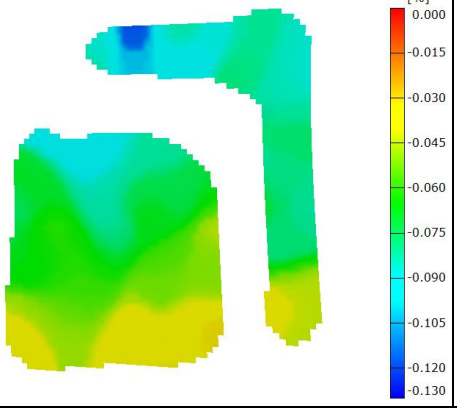	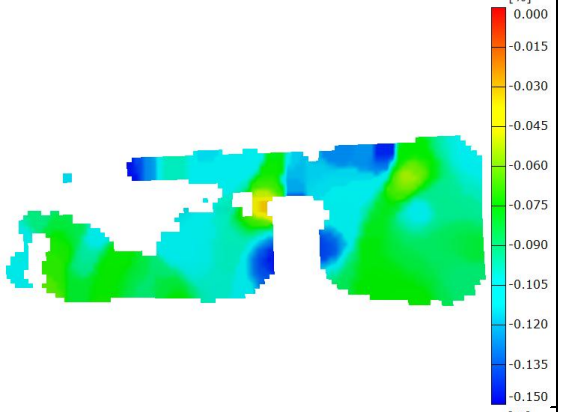
6.0m	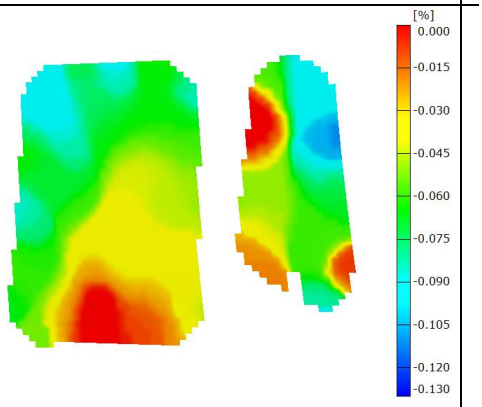	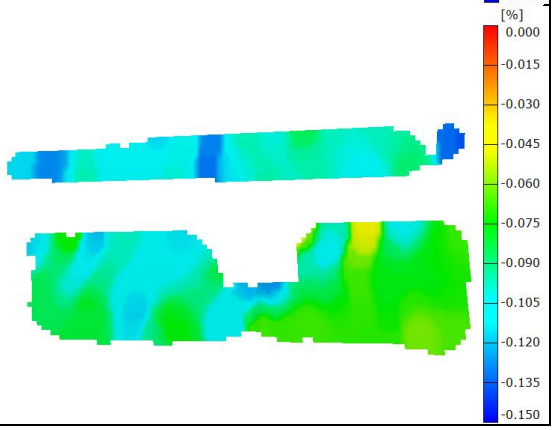

1.10 DIC TESTING OF UMASS LOWELL BLADE WITH DEFECTS

Three types of defects were embedded into the TPI Composites CX-100 9 meter wind turbine blade as previously described located on the low (bottom) and high (top) pressure side of the blade at 3.5, 5, and 6 m from the root of the blade. This section describes the results of the DIC measurement made overreach of these areas as a function of fatigue cycling.

For each measurement location, the blade was loaded upwards with a force of 325 lbs. to offset the weight of the saddle (located at 6.75 m). Therefore the only load that the blade experienced was due to its own weight. Five reference images were taken and subsequently the blade was loaded downward by applying a 518 lb. weight to the saddle. An additional five images were captured. Images were taken at one of the six defect locations in the reference (upward loaded) and loaded (downward) positions and then the cameras were repositioned. The test was repeated for each of the six defect locations at a specific number of fatigue cycles. Six sets of images were taken at a fatigue cycle count of a) 0 cycles; b) 25,603 cycles; c) 755,049 cycles; d) 1,803,350 cycles. The strain computation settings used for Aramis are shown in Table B-3.

TABLE B-3. Parameter settings for Aramis strain calculations.

Parameter	**Strain**
Facet Size	20
Facet Step	15
Computation Size	5
Filter Size	7
Filter Runs	3

The strain contour map of the six different regions for the virgin blade (0 cycles) are shown in Figure E.34. The results reveal that the defect locations are readily discernible. Each of the locations near the defect has larger than nominal strain. As the blade was cycled, the strain amplification in the vicinity of the defect became more apparent as is shown in Figure E.35 for the 5m high pressure side, defect location (area where failure first occurred). The images for the other regions are similar and have not been included in this report.

A fiber optic cable was placed (by Luna Innovations) to monitor strain along the spar cap. The DIC measurements were analyzed along the section line in the same location as the fiber optic cable for different cycle counts. The DIC results are shown in Figure E.36 for all six defect locations sampled at each of the fatigue cycle counts. Similarly, the strain along a section line in the location of the maximum strain (for different cycle counts) at all six defect locations is shown in Figure E.37. The results reveal a clear strain amplification in the vicinity of the defect that is affected by the number of fatigue cycles applied.

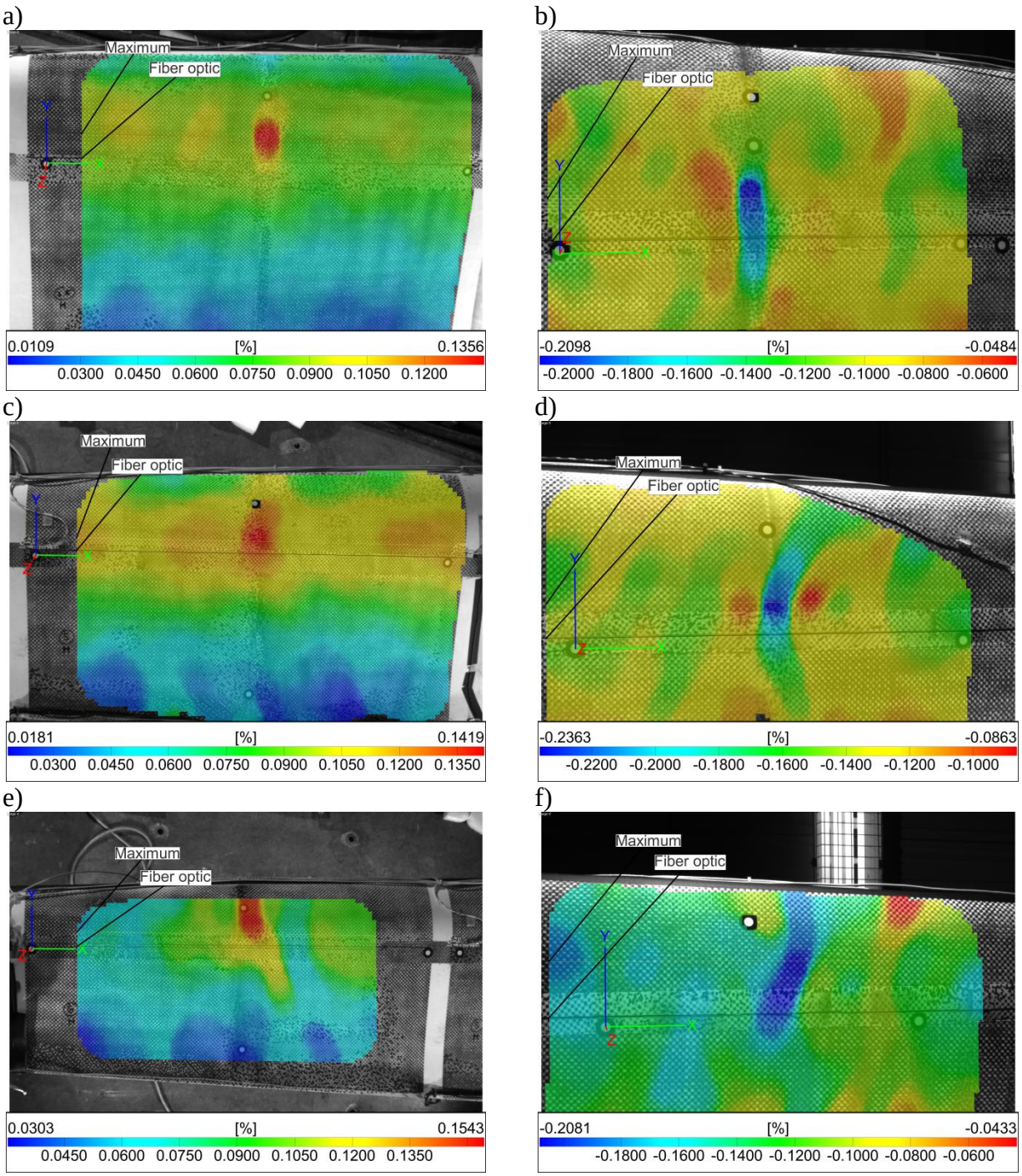

Figure E.34 Strain contour plot at 0 cycles for a) 3.5 meters, high-pressure; b) 3.5 meters, low-pressure; c) 5.0 meters, high-pressure; d) 5.0 meters, , low-pressure; e) 6.0 meters, high-pressure; f) 6.0 meters, , low-pressure.

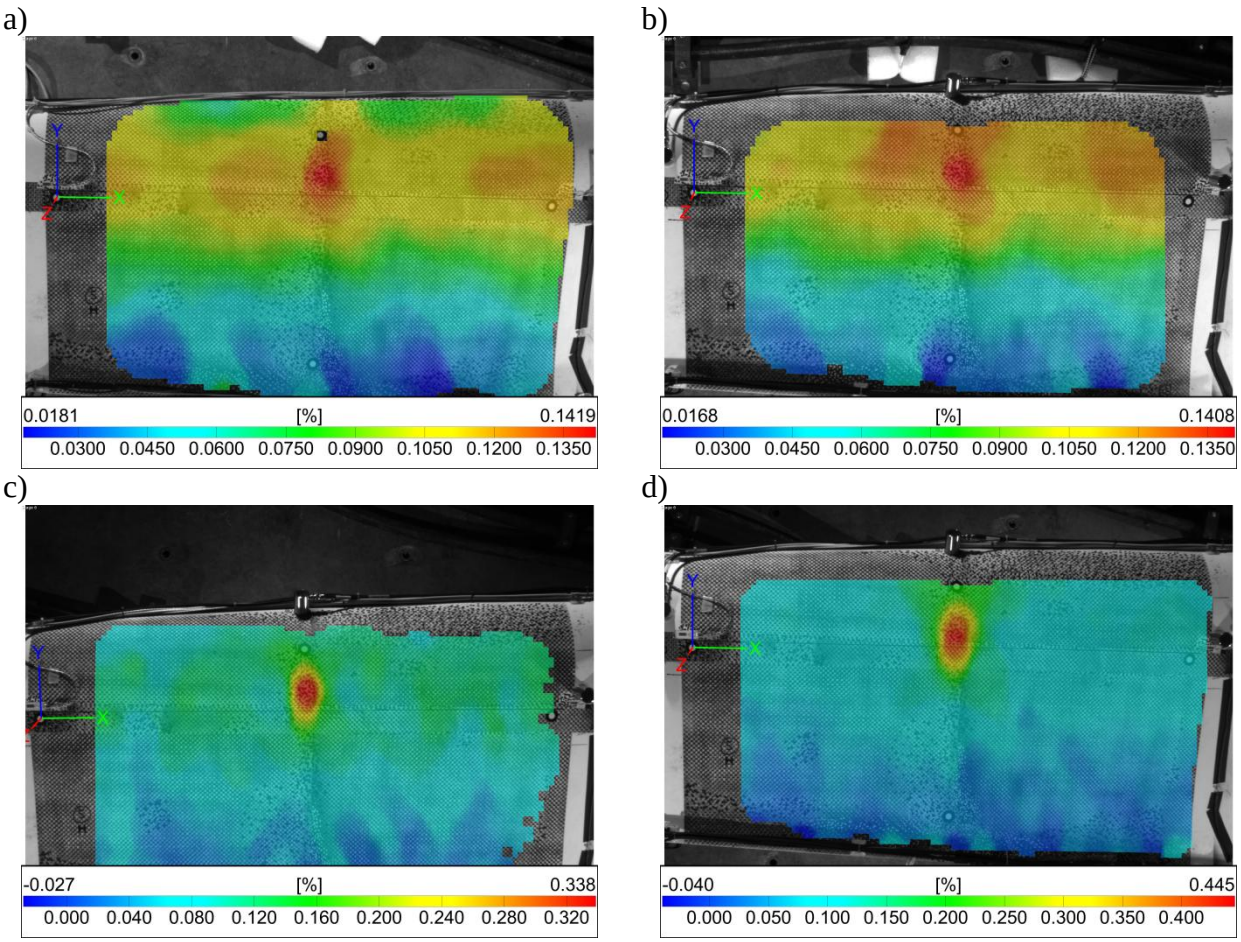

Figure E.35 Strain contour plots for the 5.0-meter section at a) 0 cycles; b) 25,603 cycles; c) 755,049 cycles; d) 1,803,350 cycles.

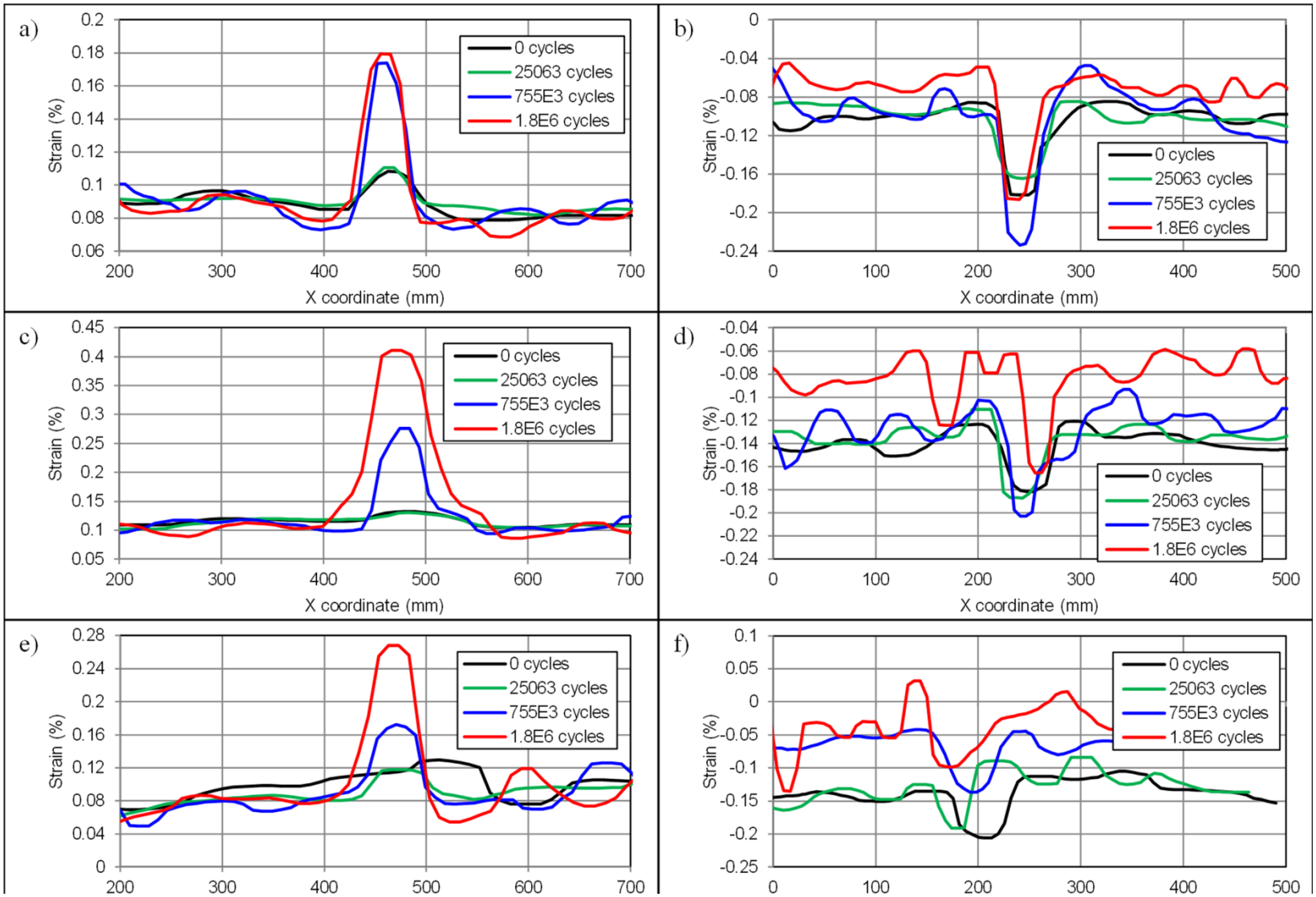

Figure E.36. Strain along fiber optic cable for different cycle counts at a) 3.5-meter, high-pressure; b) 3.5-meter, low-pressure; c) 5.0-meter, high-pressure; d) 5.0-meter, low-pressure; e) 6.0-meter, high-pressure; f) 6.0-meter, low-pressure surfaces.

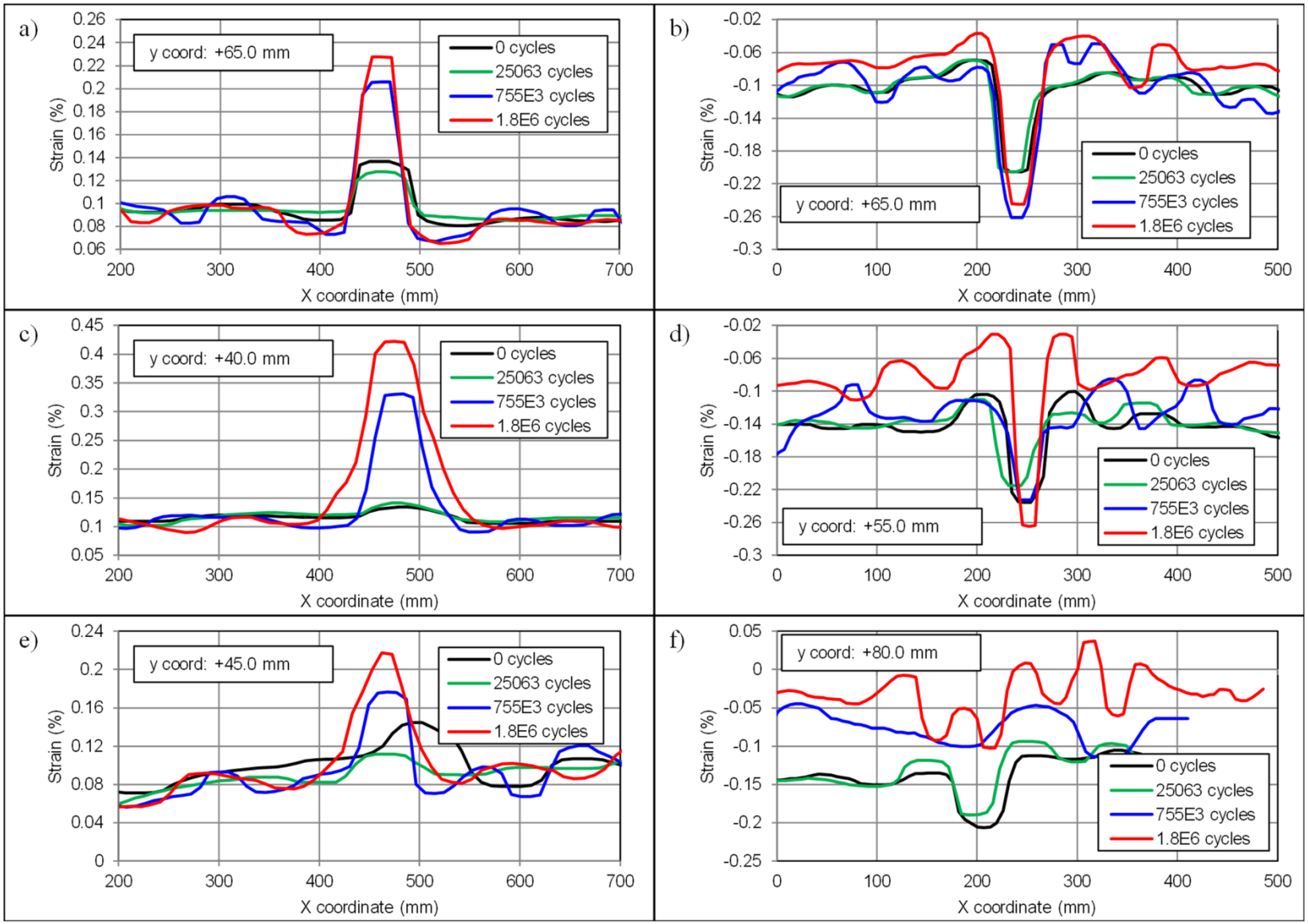

Figure E.37. Maximum strain for different cycle counts at a) 3.5-meter, high-pressure; b) 3.5-meter, low-pressure; c) 5.0-meter, high-pressure; d) 5.0-meter, low-pressure; e) 6.0-meter, high-pressure; f) 6.0-meter, low-pressure surfaces (y coordinate of section line also listed).

1.11 REFERENCES FOR APPENDIX E

1. *Digital image correlation using Newton-Raphson method of partial differential correction.* **Bruck, H. A., et al.** 3, s.l. : Experimental Mechanics, 1989, Vol. 29.
2. **Helfrick, M.** *An Investigation of 3D Digital Image Correlation for Structural Health Monitoring and Vibration Measurement.* Lowell, MA : University of Massachusetts Lowell, 2008. Master's Thesis.
3. **GOM.** *Optical Measuring Techniques.* [Online] 08 2011. [Cited: 08 14, 2011.] www.gom.com.
4. **Boresi, A. and Schmidt, R.** *Advanced Mechanics of Materials.* Hoboken, NJ : John Wiley & Sons, Inc., 2003.
5. **GOM Optical Measuring Technologies.** *ARAMIS: User Manual - Software.* Braunschweig, Germany : s.n., 2007.
6. *Structural Testing of 9 Meter Carbon Fiber Wind Turbine Research Blades.* **Paquette, J., Van Dam, J. and Hughes, S.** 2007. AIAA Conference.
7. *Structural Health Monitoring of Wind Turbine Blades.* **Rumsey, M. and Paquette, J. A.** San Diego, CA : s.n., 2008. SPIE Smart Structures and Materials & Nondestructive Evaluation and Health Monitoring.
8. *An Evaluation of Sensing Technologies in a Wind Turbine Blade.* **Rumsey, M.** San Diego, CA : s.n., 2011. SPIE Smart Structures and Materials & Nondestructive Evaluation and Health Monitoring.
9. *Sensor Projects at Sandia National Laboratories.* **Rumsey, M.** Albuquerque, NM : s.n., 2008. Sandia National Laboratories Wind Turbine Blade Workshop.

Data Management

The DIC project files are saved in an Aramis specific file structure (FILENAME.dap). For the UMass Defect Blade, project files were made for the following test cases. For each test case 5 upward loading & 5 downward loading images were taken. The data is stored on the Aramis DIC system and is backed up using portable hard drives.

Blade region (m)	0 cycles	25063 cycles	755049 cycles	1.803E6 cycles
3.5 HP				
5.0 HP				
6.0 HP				
3.5 LP				
5.0 LP				
6.0 LP				

HP (High Pressure side) and LP (Low Pressure Side)